NASA CONTRACTOR
REPORT

NASA CR-61234

May 1968

NASA CR-61234

INVESTIGATION OF HEAT TRANSFER AND PRESSURE ON FLAT PLATES AND CURVED PANELS DUE TO ROCKET EXHAUST IMPINGEMENT

By D. E. Kooker and P. O. McCormick
LOCKHEED MISSILES AND SPACE COMPANY

FACILITY FORM 602
N68-29457 (ACCESSION NUMBER)
(THRU)
64 (PAGES)
1 (CODE)
CR-61234 (NASA CR OR TMX OR AD NUMBER)
33 (CATEGORY)

AUG 1968
RECEIVED
NASA STI FACILITY
INPUT BRANCH

For

NASA-GEORGE C. MARSHALL SPACE FLIGHT CENTER
Huntsville, Alabama

May 1968 NASA CR-61234

INVESTIGATION OF HEAT TRANSFER AND PRESSURE ON FLAT PLATES AND CURVED PANELS DUE TO ROCKET EXHAUST IMPINGEMENT

By

D. E. Kooker and P. O. McCormick

Prepared under Contract No. NAS 8-20082 by

LOCKHEED MISSILES AND SPACE COMPANY
Huntsville, Alabama

For

Aero-Astrodynamics Laboratory

Distribution of this report is provided in the interest of information exchange. Responsibility for the contents resides in the author or organization that prepared it.

NASA-GEORGE C. MARSHALL SPACE FLIGHT CENTER

FOREWORD

This report presents the results of work performed by personnel of the Thermal Environment Section of the Lockheed Missiles & Space Company, Huntsville Research & Engineering Center for the Aero-Astrodynamics Laboratory of Marshall Space Flight Center under Contract NAS8-20082 (subcontract to NSL PO 5-09287). This task was conducted in response to the requirements of Appendix B-1, Schedule Order No. 104-B.

The NASA technical coordinators for this study were Mr. William C. Rochelle and Mr. Terry F. Greenwood, R-AERO-AT, of the Thermal Environment Branch of the Aero-Astrodynamics Laboratory.

SUMMARY

Experimental and theoretical correlations of pressure and heat transfer rate were obtained under a wide variety of test conditions for rocket exhausts impinging on flat plates and curved panels. Axisymmetric real gas exhaust plumes were generated using the method of characteristics and equilibrium chemistry to provide input to the heating and pressure analysis. Impingement pressures were calculated using both a relieved boundary approach and the Newtonian impact theory for strong and weak shock interaction regions. Heat transfer rates in the weak shock region were obtained using various methods, including a turbulent iteration method and the Spalding and Chi turbulent skin friction method. A modified Fay and Riddell equation was used in the strong shock region. The results showed that the experimental pressures and heating rates can be predicted quite accurately with the analyses developed.

CONTENTS

Section		Page
	FOREWORD	ii
	SUMMARY	iii
	LIST OF FIGURES	v
	NOMENCLATURE	vii
1	INTRODUCTION	1
2	EXPERIMENTAL ANALYSIS	3
3	FLAT PLATE IMPINGEMENT FLOW FIELD AND PRESSURE ANALYSIS	7
	3.1 Weak Shock Region	8
	3.2 Strong Shock Region	11
4	HEAT TRANSFER ANALYSIS	14
	4.1 Weak Shock Region	14
	4.2 Strong Shock Region	22
5	DISCUSSION OF RESULTS	24
	5.1 Pressure Distribution	24
	5.2 Heat Transfer Rate	26
6	CONCLUSIONS	29
7	REFERENCES	30
Appendix		
A	THE CONCEPT OF FAR DOWNSTREAM	A-1

LIST OF FIGURES

Figure		Page
1	Location of Instrumentation on Flat Plate for Centaur Retro Tests	35
2	Centaur Panel used in S-IVB Retro Motor Tests	36
3	S-IB/S-IVB Interstage used in S-IB Retro Tests at CAL	37
4	Flat Plate used in RDS-507 Propellant Tests at CAL	38
5	Description of Flat Plate Impingement Problem (Not to Scale)	39
6	Relationship Between Plume Volume Ratio, V_1/V_2, and Parameter, Tanθ	40
7	Relationship Between Parameter a and Parameter Tanθ	41
8	Mach Number Contours for UTC Centaur Retro Motor at 109,000 Ft	42
9	Comparison of Pressures on Flat Plate Due to Exhaust of UTC Centaur Retro Motor at 109,000 Feet	43
10	Comparison of Pressures on Flat Plate Due to Exhaust of Thiokol Centaur Retro Motor at 120,000 Feet	44
11	Comparison of Pressures on Flat Plate Due to Exhaust of RDS-507 Motor at 200,000 Feet	45
12	Comparison of Pressures on Flat Plate Due to Exhaust of Air (From Reference 2) at 166,000 Feet	46
13	Comparison of Pressures on Flat Plate Due to Exhaust of Nitrogen (From Reference 3) at 87,000 Feet	47
14	Comparison of Pressures on Centaur Panel Due to Exhaust of S-IVB Retro Motor at 115,000 Feet	48
15	Comparison of Pressures on S-IB/S-IVB Interstage Due to Exhaust of S-IB Retro Motor at 200,000 Feet	49
16	Mach Number Contours for S-IB Retro Motor at 200,000 Feet	50
17	Comparison of Total Pressure Behind Shock (Pitot Pressure) in S-IB Retro Motor Plume at 200,000 Feet	51
18	Comparison of Pressures on S-II Interstage Due to Exhaust of S-II Retro Motor at 391,000 Feet	52
19	Comparison of Heat Transfer Rates on Flat Plate Due to Exhaust of UTC Centaur Retro Motor at 109,000 Feet	53

LIST OF FIGURES (continued)

Figure Page

20 Comparison of Heat Transfer Rates on Flat Plate Due to Exhaust of Thiokol Centaur Retro Motor at 120,000 Feet 54

21 Comparison of Heat Transfer Rates on Flat Plate Due to Exhaust of RPI Centaur Retro Motor at 117,000 Feet 55

22 Comparison of Heat Transfer Rates on S-IB Interstage Due to Exhaust of S-IB Retro Motor at 200,000 Feet 56

23 Comparison of Heat Transfer Rates on Centaur Panel Due to Exhaust of S-IVB Retro Motor at 115,000 Feet 57

NOMENCLATURE

a	parameter in Equation (1)
b	parameter in Equation (1)
c	concentration
c_p	specific heat at constant pressure
C_f	skin friction coefficient
C_h	Stanton number
d_e	diameter of nozzle exit
F_c	function defined by Equation (39)
$F_{R\theta}$	function defined by Equation (40)
F_{Rx}	function equal to $F_{R\theta}/F_c$
g	acceleration due to gravity
G_1	term used in Equation (35)
h	static enthalpy; also distance of plate from nozzle axis of symmetry
$\overline{h}$	nondimensional distance equal to h/R_e
h^o	heat of formation
H	shape factor equal to $(\delta^*/\Delta)/(\theta/\Delta)$
J	mechanical equivalent of heat
Le	Lewis number
ℓ	length
M	Mach number
p	static pressure

NOMENCLATURE (continued)

Pr	Prandtl number
q	heat transfer rate
r	recovery factor
r_c	chemical recovery factor
R	gas constant; also distance perpendicular to nozzle axis of symmetry
$\overline{R}$	nondimensional distance equal to R/R_e
R_e	radius of nozzle exit
Re	Reynolds number
Re_δ	Reynolds number based on δ
T	temperature
u	velocity
u_τ	friction velocity equal to $(\tau_w/\mu_w)^{0.5}$
u_G	parameter in Equation (41) equal to $(2/C_{f_i})^{0.5}$
V_1	volume segment of plume
V_2	volume segment of axisymmetric unrelieved flow field
x	distance along plate centerline
$\overline{x}$	nondimensional distance equal to x/R_e
$\overline{x}_T$	axial location at which weak oblique shock can be attached to plate
y	distance perpendicular to plate
y_τ	friction length
γ	effective isentropic exponent
δ	boundary layer thickness; also turning angle
δ^*	displacement thickness

NOMENCLATURE (continued)

Δ	transformed boundary layer thickness
ϵ	nozzle expansion ratio; also shock angle
η	parameter in Dorodnitzen transformation
θ	momentum thickness; also flow angle
μ	viscosity
ρ	density
τ	shear stress
ϕ	correction factor equal to $(c_{i_1} - c_{i_w})/c_{i_1}$

Subscripts

AMB	ambient conditions outside plume
aw	adiabatic wall
CH	chemical
e	exit
FS	full-scale
i	species i; also incompressible
KIN	kinetic
M	model
mws	maximum strength weak shock
n	last term in iteration process
SL	sea level
ss	strong shock
t	total
T	supersonic turning point

NOMENCLATURE (continued)

Subscripts

TH	thermal
w	wall
1	properties behind shock at edge of boundary layer
∞	properties in freestream in front of shock

Superscript

$*$	properties evaluated at Eckert reference enthalpy

Section 1

INTRODUCTION

During separation of stages of large rocket vehicles, such as the Saturn, solid propellant retro and ullage motors fire in order to facilitate removal of lower stages from upper stages. Because of the high altitudes involved, the highly expanded plumes of these motors impinge upon and consequently may damage nearby components and structures on both upper and lower stages. Because of this possibility of damage, it is necessary to have suitable methods of predicting impingement heating and pressures which will compare favorably with both ground test and in-flight experimental data.

The analysis (experimental and theoretical) of plume impingement on flat plates or curved panels mounted parallel or at a small angle to the nozzle axis has received considerable attention in recent years. Bauer and Schlumpf (Reference 1) and Vick and Andrews (Reference 2) measured pressures on flat plates in which cold air was used as the working fluid. Margolin and Welch (Reference 3) and Gopin and Margolin (Reference 4), using cold nitrogen and helium and cold argon and sulfur hexafluoride, respectively, as the working fluids, also measured pressures on flat plates. Heat transfer as well as pressures were measured on a splitter plate placed between two engines of an S-IV four-engine model at Cornell Aeronautical Laboratory (CAL) (Reference 5), using gaseous H_2 and O_2 as the propellants. Experimental measurements of heating and pressure on a flat plate due to the exhaust of an Aerozine $50/N_2O_4$ Apollo RCS[†] engine were reported by Runyan (Reference 6), Barebo and Ansley (Reference 7), Piesik and Lofland (Reference 8), and Boudreaux and Etheridge (Reference 9). Lehrer (Reference 10) obtained temperature measurements on a curved panel impinged upon by exhausts of a scale model of the RCS engine. Theoretical correlations of heating and pressure for the full-scale RCS engine tests were discussed by Piesik (Reference 11) and Piesik, Koppang, and Simkin (Reference 12), as well as by Boudreaux and Etheridge (Reference 9). Other recent theoretical analyses of rocket exhaust impingements effects on a flat plate have been reported by Africano (Reference 13) and Lewis, Hackett, and Kuby (Reference 14).

[†] Reaction Control System

In recent years NASA/Marshall Space Flight Center and Lockheed/Huntsville have been investigating the effects of rocket exhaust impingement on various parts of the Saturn vehicles. Rochelle (Reference 15) presented a summary of heating and pressure instrumentation used in exhausts of both solid and liquid propellant Saturn rockets. Rochelle (Reference 16) discussed various types of heating, including stagnation and flat plate convection, particle impingement and particle radiation from Saturn ullage and retro motor exhausts. Rochelle (Reference 17) and Gibson (Reference 18) discussed an analysis of heating caused by the S-IB retro motor exhaust impinging on the S-IB/S-IVB interstage, and Rochelle (Reference 19) presented calculations of impingement pressure on the S-IC forward interstage caused by the S-II ullage motor exhaust.

In this report, analytical techniques for predicting impingement pressures and convective heating on flat plates and curved panels (or sections of the actual rocket vehicle) are discussed along with test data for a wide variety of altitudes, chamber pressures, area ratios, and distances of plate to nozzle axis as shown in Table 1 (see page 6). The majority of the experimental data analyzed pertains to solid propellant plumes; however, because of the small particle loadings (particle mass flow less than 5% of the total mass flow) and relative positions of plume axis and flat plate (or vehicle surface), the particle impingement heating rates were practically negligible.

Section 2
EXPERIMENTAL ANALYSIS

Experimental values of pressure and heat transfer rate on flat plates and curved panels immersed in a rocket exhaust plume were obtained from several test programs. This section gives a summary of the test programs which provided data for comparison with theoretical prediction methods.

Centaur Retro Test at NASA/Marshall Space Flight Center (MSFC)

This test program involved the determination of impingement pressures and heating rates from the plumes of ten motors of five types of solid propellant (two of each type) which were possible candidates for the Centaur retro motor used for separating the Centaur stage from its payload. The motors, which were of the general thrust level of 500-1000 pounds, were fired in Altitude Cell 112 (which was capable of altitude simulation of 100-120,000 feet) at MSFC's Test Laboratory. Rochelle (Reference 20) gave the overall description of the instrumentation involved and a discussion of heating (radiative as well as total) and pressures obtained during the program. Figure 1 shows the location of the heat transfer and pressure instrumentation on the aluminum flat plate which was mounted vertically in the cell, 12 inches from the axis of each motor. The heat transfer calorimeters were of the Gardon-gage (Reference 21) type, and the pressure transducers were of the absolute-unbonded strain-gage type.

S-IVB Retro Test Arnold Engineering Development Center (AEDC)

These tests involved the measurement of pressure and heat transfer on a model of the centaur stage as a result of S-IVB retro motor exhaust impingement. The test configuration (Figure 2) was mounted in the spray chamber of the 300-foot deep J-4 cell (capable of altitude simulation of 90-130,000 feet) at AEDC. Five 6100-pound thrust motors were fired in the program — three at 0° cant angle with the motor axis 37 inches from the Centaur surface, and two at 11.5° cant angle. The complete description of this test program, including various laser beam attenuation, solar cell, and paint sample degradation experiments, was given by Muse (Reference 22). Total heating rates were measured along the panel at five positions (55-125 inches from the nozzle exit) and pressures at seven positions (55-148 inches from the nozzle exit).

S-IB and S-II Retro Tests at Cornell Aeronautical Laboratory (CAL)

This test program involved the simulation of S-IB and S-II retro motors by means of a solid propellant combustor whose exhaust impinged on 1/10-scale models of the S-IB/S-IVB and S-II/S-IVB interstages, the S-IVB thrust structure, and the J-2 engine. The test configuration for the S-IB/S-IVB interstage, shown in Figure 3 with some of the heating and pressure gages in position, was mounted inside the CAL 10 x 28-foot altitude chamber. For the S-IB retro firings this cell was pumped down to a pressure simulating 200,000 feet, the approximate S-IB/S-IVB separation altitude, and for the S-II retro firings to a pressure simulating 391,000 feet (the highest simulated altitude obtainable in the cell). Heating and static pressure measurements were obtained on the interstages, S-IVB thrust structure, and J-2 engines; and total pressures were measured on the interstage by means of a five-pronged pressure rake. A description of the preliminary test plan for this program was given by Rochelle (Reference 23); Dennis and Hendershot (Reference 24) have described all of the S-IB and S-II retro pressure and heating data.

The solid propellant combustor, discussed by Hendershot (Reference 25), consists basically of a combustion chamber, exhaust nozzle, and nozzle and venting diaphragms. In the combustion chamber thin sheets of solid propellant were glued to a 10-point star propellant holder. Uniform propellant burning in the chamber was accomplished within 2-3 milliseconds by a spark-ignited oxygen-rich (O/F = 20) H_2-O_2 mixture. After the nozzle diaphragm ruptured at the design pressure of about 1700 psia, approximately 10-15 milliseconds of steady state testing time existed for each run. Extremely fast-response pressure (Reference 26) and platinum thin-film heat transfer (Reference 27) instrumentation were used to make all measurements.

Rocketdyne RDS-507 Propellant Test at Cornell Aeronautical Laboratory (CAL)

The short-duration combustor described above, and discussed by Hendershot in Reference 28, was used in this test. A 28-inch x 28-inch flat plate, shown in Figure 4, was mounted 4.5 inches from the axis of a motor which used Rocketdyne RDS-507 propellant and which had about 10% Al_2O_3 particles in the exhaust. Fast-response pressure gages were used to obtain measurements at ten locations off the centerline. Fast-response platinum thin-film gages were used at eight positions on the plate centerline and at six locations off the plate centerline.

Other Sources of Data

Heating rate correlations were made for the S-I interstage and S-IV stage thermocouple data discussed by Usher (Reference 29). These data were obtained while the S-I retro motor exhaust impinged on these areas during the flight of the Saturn SA-3 vehicle. Total heating calorimeter data on the S-IB interstage caused by impingement of the S-IB retro exhaust during flights of the Saturn AS-201 and 202 vehicles was used to correlate with CAL tests and theoretical calculations. Pressure correlations were made for some of the cold gas data of References 1, 2 and 3, and both heating and pressure correlations were determined for some of the data discussed in References 11 and 12.

A summary of the important parameters associated with each experimental test program considered in the present report is shown in Table 1 for reference purposes.

Table 1
TEST DATA ANALYZED

Motor	Test Location	d_e (in.)	A_e/A_{th}	p_c (psia)	Alt. (Kft)	$\bar{h}$	p_{t_e}/p_{AMB}
S-IB Retro	CAL	0.89[a]	4.26	1770	200	b	6.74×10^5
S-II Retro	CAL	0.89[a]	4.26	1770	391	b	6.23×10^9
Thiokol Cent. Retro	MSFC	1.189	2.80	1100	120	20.18	1.57×10^4
UTC Cent. Retro	MSFC	2.406	12.60	1700	109	9.97	1.58×10^4
RPI Cent. Retro	MSFC	2.05	7.20	640	117	11.7	8.10×10^3
S-IVB Retro	AEDC	4.67	4.81	1070	115	15.82	1.26×10^4
RDS-507	CAL	1.932	26.60	1060	200	4.65	3.15×10^5
S-1 Retro	SA-3	11.62	6.67	1000	235	b	1.55×10^6
Cold Gas (Ref. 1)[c]	AEDC	0.400	1.688	450	114	7.25	5.06×10^3
Cold Gas (Ref. 2)[c]	Langley	0.625	25.2	2400	166	12.0	2.00×10^5
Cold Gas (Ref. 3)[c]	NAA	0.354	2.0	650	87.5	2.0	2.34×10^3
Apollo RCS (Ref. 11)[c]	AEDC	2.744	10.0	90	230	3.0	1.14×10^5

---

[a] 0.10 scale test

[b] variable

[c] not sponsored by MSFC

Section 3

FLAT PLATE IMPINGEMENT FLOW FIELD AND PRESSURE ANALYSIS

The flow field created by a rocket nozzle exhaust plume impinging upon a flat plate boundary parallel to the nozzle axis of symmetry (hereafter called the impingement flow field) can be solved exactly by a three-dimensional method. However, the absence of a good three-dimensional method which adequately describes all the aspects of this complex problem has prompted a search for a simple but reliable method based on existing capabilities. The initial problem of describing a real gas nozzle exhaust plume flow field can be solved accurately by the Lockheed/Huntsville method-of-characteristics solution (Reference 30) as demonstrated in Reference 31. The NASA/Lewis thermochemistry program which can handle either frozen or equilibrium chemistry has been incorporated as part of Reference 30. The present analysis makes use of this method and the equilibrium assumption to generate an axisymmetric exhaust plume flow field at the prescribed altitude for each rocket motor, based on the given propellant composition and chamber pressure.

Looking at the impingement flow field from a simplified point of view, the flow along the centerline of the flat plate boundary might be envisioned as essentially two-dimensional. However, if the undisturbed plume flow field is to be described by an axisymmetric method of characteristics solution, a start line from an axisymmetric method-of-characteristics flow field cannot be used to generate a two-dimensional impingement flow field. Thus, an impingement flow field based on the axisymmetric plume must itself be axisymmetric. Of course, in the physical problem, the impingement flow field along the centerline is neither two-dimensional nor axisymmetric due to the three-dimensional "relief" which occurs as the flow spreads over the flat plate. However, by using an axisymmetric impingement flow field, this relief may be simulated by appropriately altering the boundary on which the method-of-characteristics solution converges. The exact form of this relieved boundary is discussed below. It should be mentioned that a three-dimensional method for predicting a pressure distribution over the plane of symmetry between axially parallel rocket nozzle exhaust plumes has been developed by D'Attore, et al.(Reference 32). The finite difference technique used to calculate the inviscid three-dimensional interaction region is based on the original method of Lax and Wendroff (Reference 33) and modified by a faster, two-step method discussed by Richtmeyer (Reference 34). In addition to the fact that the flow medium is treated as an ideal gas, however, the method will handle only weak interactions between the adjacent plumes; i.e., no subsonic regions are allowed. These restrictions, along with the need for initial information from a characteristics program, limit the usefulness of the method.

3.1 WEAK SHOCK REGION

An important factor in determining the impingement flow field is separating the supersonic and subsonic flow regions. The shock wave generated by the plume flow field impinging on the flat plate boundary will lie approximately parallel to the boundary for a short distance down the plate. (See Figure 5.) The portion of the impingement flow field behind this normal shock, similar to that found in the stagnation region of a blunt body, is subsonic and cannot be predicted by the method of characteristics. At some point downstream, however, the Mach number becomes greater than unity and the impingement shock wave curves away from the boundary in accordance with weak shock wave theory. A start line for the method of characteristics may be determined by superposing the flat plate boundary upon the exhaust plume flow field and tracing each left running characteristic line as it crosses the boundary. Beginning with the point at which the envelope shock crosses the boundary, a decision can be made for each characteristic line whether or not the maximum strength weak shock could be attached artificially at the crossing point. The point on the boundary closest to the nozzle exit plane at which the maximum strength weak shock can be attached and sustain supersonic flow downstream is designated the "turning point," and the characteristic line passing through this point becomes the "start" line for the method-of-characteristics impingement flow field.

It is fully realized that in the physical flow field, the weak portion of the shock wave is not attached to the boundary. Observation of experimental flow fields indicates, however, that the actual shock wave becomes tangent to the artificially attached shock wave after a very short distance. Thus, use of an artificial attachment point simplifies the start of the supersonic portion of the flow field (weak shock region) while introducing errors of only negligible importance. This will be verified by comparing predicted pressure on the boundary and experimental data in this region.

With the start line now defined, and the flat plate boundary assumed to be unaltered, the axisymmetric impingement flow field becomes the flow inside a cylinder of radius equal to the distance between the plate and the nozzle axis of symmetry. However, this flow field would account for none of the three-dimensional relief effects which are present in the physical problem. By examining the comparison between several method-of characteristics impingement flow fields and the corresponding test data for pressure distribution on the flat plate centerline, it was determined that an altered or fictitious upper boundary represented by a cubic equation would predict the data. In terms of nondimensional coordinates, this equation is given by

$$(\bar{R} - \bar{h})^3 + a\,(\bar{R} - \bar{h})\,(\bar{x} - \bar{x}_o) - b\,(\bar{x} - \bar{x}_o)^3 = 0 \tag{1}$$

where $\bar{x}_o$ is the axial location where Newtonian impact theory predicts a maximum value of pressure on the flat plate boundary. Although Newtonian impact theory,

$$p_{body} = p_\infty + \rho_\infty u_\infty^2 \sin^2\left[\theta_{flow} - \theta_{body}\right] \tag{2}$$

predicts the correct location of the maximum pressure in the weak shock region, it fails to give the correct magnitude of the maximum and the shape of the distribution curve.

The parameters a and b are unique for each problem and can be determined in the following manner. The quantity,

$$\tan\theta = b^{1/3} \quad (b > 0) \tag{3}$$

defines the slope of a line to which Equation (1) asymptotically becomes tangent for values of $\overline{x}$ beyond a certain point. In a sense, this angle θ represents the maximum amount of relief needed to simulate the physical flow problem far downstream. For the range of parameters considered in the present report, the axial location ($\overline{x}_T + 30$) can be treated as far downstream i.e., a point beyond which the derivative of Equation (1) is asymptotically close to Equation (3). This idea is further illustrated by several representative examples shown in Appendix A. Another measure of this flow relief can be defined in terms of a volume ratio. A volume segment of the plume may be calculated from $\overline{x}_T$ to $\overline{x}_T + 30$ between the plume free boundary and the flat plate boundary, where the flat plate is a plane defined by $\overline{R} = \overline{h}$. If this volume segment is V_1 and the volume of the axisymmetric unrelieved flow field is defined as

$$V_2 = \pi \overline{h}^2 \left[(\overline{x}_T + 30) - \overline{x}_T \right] = 30 \pi \overline{h}^2 \tag{4}$$

the volume ratio V_1/V_2 then represents the need for relief based on the volume of the exhaust plume which is intercepted by the flat plate boundary. An empirically derived relationship between these two measures of relief, V_1/V_2 and $\tan\theta$, is given by Figure 6. The relationship between the parameter a and $\tan\theta$, is given by Figure 7.

Thus, a given rocket motor, propellant composition, chamber pressure, altitude (P_{AMB}), and the flat plate location specify a supersonic turning point and volume ratio V_1/V_2. The value of V_1/V_2 determines a unique value of the parameter $\tan\theta$ by Figure 6, and Figure 7 specifies the unique value of the parameter a associated with the value of $\tan\theta$. A calculation of Newtonian impact pressure [Equation (2)] along the flat plate boundary based on the flow field properties in the method of characteristics undisturbed plume flow field will yield $\overline{x}_o$, the axial location of the maximum Newtonian pressure. The value of these parameters in Equation (1) determined the relieved boundary for the axisymmetric method of characteristics impingement flow field. Then the pressure predicted on the relieved boundary of the impingement flow field becomes the pressure on the actual flat plate centerline at the same axial location.

3.2 STRONG SHOCK REGION

The region of the impingement flow field upstream of the turning point is difficult to analyze. Depending on the strength of the plume and the relative location of the plate with respect to the axis of symmetry, a certain amount of flow reversal can be present. However, a good approximation of the pressure distribution and heat transfer rates on the flat plate boundary in this region can be determined without a detailed knowledge of the actual flow field.

The method used in this analysis to determine the pressure on the flat plate in the region where the impingement shock wave is roughly parallel to the boundary (hereafter called the strong shock region) is based on ideal gas shock relations. It is postulated that the flow must turn through a strong shock wave such that it becomes parallel to the boundary. With the flat plate superposed on the exhaust plume flow field, flow field properties can be determined at each point where a characteristic line crosses the flat plate, beginning with the intersection of the undisturbed plume free boundary. The values of Mach number and γ at each intersection point are used as upstream conditions to define the turning angle and shock angle associated with the maximum strength weak shock wave at that point. Then, the strong shock wave which is hypothesized to exist at this point is assumed to have a shock angle and turning angle less than or equal to those for a normal shock wave but greater than those for the maximum strength weak shock wave. Since the turning angle for the strong shock wave has been defined as the difference between the flow angle and the boundary angle, only the shock angle must be determined. This is done with a linear interpolation formula

$$\frac{\epsilon_{ss} - \epsilon_{mws}}{\epsilon_{normal} - \epsilon_{mws}} = \frac{\delta_{ss} - \delta_{mws}}{\delta_{normal} - \delta_{mws}}$$

or

$$\epsilon_{ss} = \epsilon_{mws} + \frac{\delta_{ss} - \delta_{mws}}{\frac{\pi}{2} - \delta_{mws}} \left(\frac{\pi}{2} - \epsilon_{mws}\right) \tag{5}$$

With the shock angle now specified, ideal gas shock relations, based on the intersection point values of Mach number, γ and static pressure as upstream properties, can be used to predict the static pressure behind the strong shock wave. It is assumed that this downstream value of static pressure is felt by the flat plate boundary. This procedure is used for each characteristic line intersection point along the flat plate between the undisturbed plume free boundary and the previously determined supersonic turning point.

Section 4
HEAT TRANSFER ANALYSIS

The analysis of heat transfer along a flat plate caused by rocket exhaust impingement is complex since the boundary layer is composed of an arbitrary gas mixture which may be dissociating and ionizing at finite chemical reaction rates (nonequlibrium flow). Also, the atoms and ions may diffuse through the boundary layer, releasing a high exothermic energy upon recombination at the wall. Furthermore, the wall may not be completely catalytic, in which case the atoms and ions would not be instantaneously recombined upon reaching the wall, and a finite number would exist there.

Because of the complexities associated with analyzing nonequilibrium boundary layers, the following equation for heat transfer through an equilibrium chemically reacting boundary layer to a flat plate, as discussed by Dorrance (Reference 35) and Rosner (Reference 36), was used in this analysis

$$q_w = C_h \rho_1 u_1 (h_{aw} - h_w) \left[1 + (Le^{2/3} - 1) \frac{\sum_i \phi c_{i_1} h_i^o}{(h_{aw} - h_w)} \right] . \qquad (6)$$

The quantity ϕ, described by Rosner (Reference 36) and Goulard (Reference 37), is defined as

$$\phi = \frac{c_{i_1} - c_{i_w}}{c_{i_1}} \qquad (7)$$

and represents a correction factor specifying the degree of catalycity at the wall. As applied to a binary dissociating gas, $\phi = 1$ implies that there are no recombined atoms at the wall and the heat transferred to the wall is a maximum (catalytic wall). Conversely, $\phi = 0$ implies that the same number of atoms exist at the wall as at the edge of the boundary layer, in which case the heat transferred to the wall is a minimum (non-catalytic wall). The assumption of $\phi = 1$ was used in this analysis. The enthalpy difference or driving potential $(h_{aw} - h_w)$ may then be written as

$$\begin{aligned} h_{aw} - h_w &= h_{1_{TH}} + h_{1_{KIN}} + h_{1_{CH}} - h_{w_{TH}} - h_{w_{CH}} \\ &= \sum_i c_{i_1} \int_{298^\circ K}^{T_1} c_{p_i} \, dT + r \frac{u_1^2}{2gJ} + r_c \sum_i c_{i_1} h_i^o \\ &- \sum_i c_{i_w} \int_{298^\circ K}^{T_w} c_{p_i} \, dT - r_c \sum_i c_{i_w} h_i^o \end{aligned} \tag{8}$$

The chemical recovery factor, r_c, discussed by Bartz (Reference 38) may be expressed as $Le^{0.6}$, where the Lewis number, Le, relates the atom diffusion through the boundary layer to the thermal diffusion of heat by conduction. The thermal recovery factor, r, was taken to be $(Pr^*)^{0.5}$ for laminar flow and $(Pr^*)^{0.333}$ for turbulent flow. In the remainder of this section a discussion will be given of both laminar and turbulent flow heat transfer prediction methods used in the weak shock region and laminar methods for the strong shock region.

4.1 WEAK SHOCK REGION

Laminar Flow. One of the laminar flow methods used in the analysis (designated the iteration method) was based upon the von Karman-Pohlhausen equation, modified for compressible flow by the Dorodnitzen transformation and programmed originally by Hoenig (Reference 39). With this method the following velocity profile was used across the laminar boundary layer

$$\frac{u}{u_1} = 2\eta - 2\eta^3 + \eta^4 + \frac{\lambda}{6}(\eta - 3\eta^2 + 3\eta^3 - \eta^4) \tag{9}$$

where the parameter λ is defined as

$$\lambda = \frac{\Delta^2}{\mu_w} \frac{\rho_1^3}{\rho_w^2} \frac{du_1}{dx} \tag{10}$$

The quantity η is obtained from the Dorodnitzen transformation as

$$\eta = \frac{1}{\Delta} \int_0^\delta (\rho/\rho_1)\, dy \tag{11}$$

The transformed boundary layer thickness, Δ, is obtained from the ratio

$$\frac{\theta}{\Delta} = \int_0^1 (1 - \frac{u}{u_1}) \frac{u}{u_1}\, d\eta \tag{12}$$

where Equation (9) is used for u/u_1.

The momentum thickness, θ, together with the skin friction coefficient, C_f, is found by an iteration of the von Karman integral equation

$$\frac{d\theta}{dx} = \frac{C_f}{2} - \theta \left[\frac{(2+H)}{u_1} \frac{du_1}{dx} + \frac{1}{\rho_1} \frac{d\rho_1}{dx} \right] \tag{13}$$

the skin friction relation

$$C_f = \frac{2\, \rho_w\, \rho_w\, (2 + \frac{\lambda}{6})}{\rho_1^2\, u_1\, \Delta} \tag{14}$$

and the transformed displacement thickness ratio

$$\delta^*/\Delta = \int_0^1 \left[\left(h/h_1\right)_{TH} - u/u_1 \right] d\eta \tag{15}$$

The enthalpy distribution through the boundary layer is found as

$$h = h_w + \left(h_{t_1} - h_w\right)\left(2\eta - 2\eta^3 + \eta^4\right) - \frac{u^2}{2gJ} \tag{16}$$

The shape factor, H, in Equation (13) is

$$H = \frac{\delta^*/\Delta}{\theta/\Delta} \tag{17}$$

The Reynolds analogy factor

$$C_h = 0.5\, C_f/(Pr_n^*)^{0.67} \tag{18}$$

was then used together with Equations (6) and (8) to predict the heating rate to the wall.

The iterative value of Prandtl number, Pr_n^*, was evaluated at the Eckert (Reference 40) reference enthalpy

$$h_n^* = 0.5\,(h_1 + h_w) + 0.22\,(Pr_n^*)^{0.5}\,(u_1^2/2gJ) \tag{19}$$

An iteration technique was used to find Pr_n^* which involved the use of the NASA/Lewis transport property program, described by Svehla (Reference 41) for an $H_2 - O_2$ system. In this manner the Lockheed/Huntsville method-of-characteristics program was used to obtain the freestream pressure, p_1, and temperature, T_1, at the edge of the boundary layer (behind the weak shock), and the Prandtl number was obtained for these two independent variables. The NASA/Lewis thermochemical program was then used to obtain the enthalpy corresponding to this temperature and pressure. These values of Prandtl number and enthalpy, h, were inserted in Equation (19) to obtain a new value of h^*. The temperature corresponding to this value of h^* was then used with the same pressure to obtain a new value of Pr^* from the transport property program and, hence, with Equation (19) a new value of reference enthalpy. The iteration process was continued until $Pr_n^* \approx Pr_{n-1}^*$ and therefore $h_n^* \approx h_{n-1}^*$.

Laminar flow theory also considered the skin friction coefficient equation due to Blasius. Using the Eckert reference enthalpy to evaluate values of μ^* and ρ^* this relation is given by

$$C_f = 0.664/\left(Re^*\right)^{0.5} = 0.664/\left(\rho^* u_1 x/\mu^*\right)^{0.5} \tag{20}$$

Equations (6), (8), (18) and (20) were then combined to obtain the heat transfer to the wall.

Another equation valid for laminar flow and compared to experimental data in the present report is a modification of the van Driest (Reference 42) equation, as discussed by Piesik, Koppang and Simkin (Reference 12). In terms of heat transfer to the wall, this can be written as

$$q_w = \frac{1.49 \times 10^{-9}}{\left(\rho_{SL_{AIR}} x\right)^{0.5}} \left[1 + \frac{5}{0.85 M_1^2}\left(1 - \frac{T_w}{T_1}\right)\right] T_1^{0.383} \rho_1^{0.5} u_1^{2.39} \tag{21}$$

Turbulent Flow. One of the turbulent flow methods used in the analysis (designated the iteration method) involved a combination of the law of the wall for incompressible flow

$$\frac{u}{u_\tau} = A \log_{10}\left(\frac{y u_\tau \rho}{\mu}\right) + C \tag{22}$$

and the velocity defect law for incompressible flow

$$\frac{u - u_1}{u_\tau} = A \log_{10}(y/\delta) + B \tag{23}$$

to obtain the skin friction relation

$$\left(\frac{2}{C_f}\right)^{0.5} = A \log_{10}\left[Re_\delta \left(\frac{C_f}{2}\right)^{0.5}\right] + C - B \tag{24}$$

where the friction velocity, u_τ, is defined as

$$u_\tau = (\tau_w/\rho_w)^{0.5} \tag{25}$$

The skin friction relation in Equation (24) was modified for compressible flow by evaluating properties at Eckert's reference enthalpy [Equation (19)], such that

$$C_f^* = C_f\,(\rho_1/\rho^*) \cong C_f\left(\frac{h^*}{h_1}\right)_{TH} \tag{26}$$

and

$$Re_\delta^* = \frac{\rho^*\, u_1\, \delta}{\mu^*} \tag{27}$$

where the thermal enthalpy ratio is given by

$$\left(\frac{h^*}{h_1}\right)_{TH} = \sum_i c_i^* \int_{298^\circ K}^{T^*} c_{p_i}\, dT \Bigg/ \sum_i c_{i_1} \int_{298^\circ K}^{T_1} c_{p_i}\, dT \tag{28}$$

Thus Equation (24) takes the form

$$\left(\frac{2}{C_f^*}\right)^{0.5} = A\left(\frac{h^*}{h_1}\right)_{TH}^{0.5} \log_{10}\left\{Re_\delta^*\left[\left(\frac{C_f}{2}\right)\left(\frac{h^*}{h_1}\right)\right]^{0.5}\right\} + (C - B)\left(\frac{h^*}{h_1}\right)_{TH}^{0.5} \tag{29}$$

Based on the analysis of Clauser (Reference 43) and others, the constants A and B are 5.6 and -2.5, respectively. The parameter, C, is obtained from Danberg's (Reference 44) data as

$$C = 5.5 + 6.4\left(1 - \frac{T_w}{T_{aw}}\right) \cong 5.5 + 6.4\left[1 - \left(\frac{h_w}{h_{aw}}\right)_{TH}\right] \tag{30}$$

where the thermal enthalpy ratio $\left(h_w/h_{aw}\right)_{TH}$ is

$$\left(\frac{h_w}{h_{aw}}\right)_{TH} = \sum_i c_{i_w} \int_{298^\circ K}^{T_w} c_{p_i}\, dT \Bigg/ \left[\sum_i c_{i_1} \int_{298^\circ K}^{T_1} c_{p_i}\, dT + \left(P_{r_n}^*\right)^{0.5} \frac{u_1^2}{2gJ}\right] \tag{31}$$

The final relation for skin friction coefficient now becomes

$$\left(\frac{2}{C_f^*}\right)^{0.5} = 5.6 \left(\frac{h^*}{h_1}\right)_{TH} \log_{10} \left\{ Re_\delta^* \left[\left(\frac{C_f}{2}\right)\left(\frac{h^*}{h_1}\right)_{TH}\right]^{0.5} \right\} + \left\{8.0 + 6.4 \left[1 - \left(\frac{h_w}{h_{aw}}\right)_{TH}\right]\right\}\left(\frac{h^*}{h_1}\right)_{TH}^{0.5} \tag{32}$$

The boundary layer thickness δ (for use in Re_δ^*) is obtained from the momentum thickness ratio equation

$$\theta/\delta = \int_0^1 \left(1 - \frac{u}{u_1}\right) \frac{\rho u}{\rho_1 u_1}\, d(y/\delta) = \int_0^1 \left(1 - \frac{u}{u_1}\right)\left(\frac{h_1}{h}\right)_{TH} \frac{u}{u_1}\, d(y/\delta) \tag{33}$$

The momentum thickness θ is found from an iteration process involving Equations (33), (32), (13), and the following equation for the displacement thickness ratio

$$\delta^*/\delta = \int_0^1 \left[1 - \left(\frac{h_1}{h}\right)_{TH} \frac{u}{u_1}\right] d(y/\delta) \tag{34}$$

The velocity variation across the turbulent boundary layer is found from the following modification of the velocity defect equation which includes the deviation from the logarithmic line

$$\frac{u}{u_1} = 1 + \frac{u_\tau}{u_1}\left[5.6 \log_{10}(y/\delta) - 2.5 + G_1(y/\delta)\right] \tag{35}$$

where the G_1 term is plotted by Clauser (Reference 43) as a function of y/δ.

The enthalpy variation is given by the Crocco equation, modified to include the Prandtl number in the expression for h_{aw}

$$h = h_w + (h_{aw} - h_w)(u/u_1) - (h_{aw} - h_w)(u/u_1)^2 \tag{36}$$

The Reynolds analogy expression is given by Shapiro (Reference 45) as

$$C_h = 0.5\, C_f / \left[1 - (1 - Pr^*)\, u_\tau (C_f/2)^{0.5}\right] \tag{37}$$

In the laminar sublayer, the friction velocity, u_τ, is equal to the friction length or friction distance parameter, y_τ, which for compressible flow with heat transferred to the wall may be written from Harkness (Reference 46) as

$$u_\tau = y_\tau = \frac{y}{\mu_w} (\rho_w \tau_w)^{0.5} = 11.5 + 6.6 \left(\frac{T_{aw} - T_w}{T_{aw}}\right) \approx 11.5 + 6.6 \left(\frac{h_{aw} - h_w}{h_{aw}}\right)_{TH} \tag{38}$$

The heating rate for turbulent flow by the "iteration" method is thus found by combining Equation (38) with Equations (37), (33), (32), (8) and (6).

Another recent and promising approach to the prediction of the skin friction coefficient in compressible turbulent flow is the calculation procedure developed by Spalding and Chi (Reference 47). They have postulated that a unique relationship exists between $F_c\, C_f$ and $F_{R\theta}\, Re_\theta$ or $F_{Rx}\, Re_x$, such that for a compressible turbulent flow, functions of Mach number and temperature alone, viz. F_c, $F_{R\theta}$, and F_{Rx}, may be found which relate the compressible flow identically to the incompressible one. Spalding and Chi concluded that the function F_c can be found from,

$$F_c = \left[\int_0^1 (\rho/\rho_1)^{1/2}\, d\,(u/u_1)\right]^{-2.0} \tag{39}$$

where the modified Crocco relation [Equation (36)] defines the enthalpy profile, which in turn provides the required density ratio. Based on the best fit of available experimental heat transfer data, they obtain for $F_{R\theta}$

$$F_{R\theta} = \left(T_{aw}/T_w\right)^{0.772} \Big/ \left(T_w/T_\infty\right)^{0.702} \tag{40}$$

and the fact that $F_{Rx} = F_{R\theta}/F_c$. Either of the functions F_{Rx} or $F_{R\theta}$ can be used in the calculation procedure depending on whether the Reynolds number is based on momentum thickness θ or running length x. Equation (40) was modified slightly due to the high adiabatic wall temperatures encountered in this analysis, and $F_{R\theta}$ was calculated in terms of thermal enthalpy ratios.

The unique relation between skin friction coefficient and Reynolds number based on momentum thickness for an incompressible turbulent boundary layer is given by Spalding (Reference 48) as,

$$\begin{aligned} Re_{\theta i} = \frac{1}{6}(u_G)^2 + \frac{1}{4.8}\Bigg\{&\left[1 - \left(\frac{2}{0.4\,u_G}\right)\right]\exp(0.4\,u_G) + \left(\frac{2}{0.4\,u_G}\right) + 1 \\ &- \frac{1}{6}(0.4\,u_G)^2 - \frac{1}{12}(0.4\,u_G)^3 - \frac{1}{40}(0.4\,u_G)^4 - \frac{1}{180}(0.4\,u_G)^5\Bigg\} \end{aligned} \tag{41}$$

Thus, assuming Spalding and Chi's hypothesis, Equation (41) can be used for compressible turbulent boundary layers by letting

$$C_{f_i} = F_c\,C_f \quad \text{and} \quad Re_{\theta i} = F_{R\theta}\,Re_\theta \tag{42}$$

where C_f and Re_θ are valid in the compressible problem.

In the present heat transfer analysis, an iteration scheme, using Spalding and Chi's skin friction hypothesis, was set up to solve for momentum thickness, θ, involving Equations (13), (33), (34) and (41). The heat transfer rates were then found by combining Equations (6), (8), (37), and the value of C_f from Equation (41).

For purposes of comparison, the turbulent heat transfer analysis also included the Blasius relation for skin friction coefficient as given by Eckert (Reference 40), using the reference enthalpy concept

$$C_f = 0.0592\,(Re^*)^{-0.2} \tag{43}$$

4.2 STRONG SHOCK REGION

In the strong shock region of plume impingement on a flat plate, some form of stagnation heat transfer relation is suggested. However, because of the infinite radius associated with a flat plate or a large radius associated with a curved panel, methods of predicting velocity gradients by the Newtonian flow relation are inaccurate (since heating rates vary as the inverse of the radius squared). Also, since this region is usually so narrow on the plate, sufficient experimental data in this region are usually lacking.

Two relations were tried for this strong shock region. One was a modification of the Fay and Riddell (Reference 49) stagnation point equation

$$q_w = \frac{0.763}{(Pr^*)^{0.6}} \left(\frac{\rho_w\,\mu_w}{\rho_1\,\mu_1}\right)^{0.1} (\rho_1\,\mu_1)^{0.5} \left[1 + (Le^{0.52} - 1)\,\frac{\sum_i \phi\, c_{i_1}\, h_i^o}{(h_{aw} - h_w)}\right] \left(\frac{\Delta u_1}{\Delta x}\right)^{0.5} (h_{aw} - h_w) \tag{44}$$

where the velocity gradient was taken to be the actual gradient behind the strong shock along the plate, starting from the point at which the plume boundary first hit the plate. The velocity u_1 and density ρ_1 in this region were those calculated by ideal gas relations behind the strong shock as discussed in the section describing the strong shock pressures. The viscosity μ_1, Lewis number Le, concentrations c_{i_1}, and adiabatic wall enthalpy h_{aw} were based upon p_1 and T_1 in this region.

The other equation used in this strong shock region was that given by Africano (Reference 13) which was a modified version of the relationship given by Kemp and Riddell (Reference 50)

$$q_w = \frac{55{,}000\ (p_1/R_1\ T_1)^{0.5}}{\epsilon + 0.75\ h/R_e} \left(1 - \frac{T_1}{T_{t_1}}\right)^{1.625} \left(1 - \frac{T_w}{T_{t_1}}\right) \qquad (45)$$

The results of these two expressions for heat transfer rate in the strong shock region and the previously described methods for predicting heat transfer rate in the weak shock region based on both a laminar and turbulent boundary layer are compared to experimental data in the next section. Although comparisons are not shown for all the test programs indicated in Table 1, the examples chosen are representative of the overall results.

Section 5
DISCUSSION OF RESULTS

5.1 PRESSURE DISTRIBUTION

A representative example of the impingement flow field created by a rocket nozzle exhaust plume impinging on a flat plate parallel to the plume axis of symmetry is shown in Figure 8 for the UTC Centaur Retro Motor at an altitude of 109,000 feet. The analytical results for pressure distribution along the centerline of a flat plate boundary, with the same configuration as illustrated in Figure 8, are compared to experimental data for five typical cases (see Figures 9 through 13). The first three cases are hot gas tests and were analyzed using the given propellant composition; the cases shown in Figures 12 and 13 are based on room temperature air and nitrogen, respectively, as the exhaust gas. For all these cases, the prediction of pressure in the weak shock region is based on results of an axisymmetric method-of-characteristics impingement flow field with a relieved boundary of the form specified by the value of the parameters a and $\tan\theta$ shown on each figure. The pressures shown in the strong shock region were predicted with the ideal gas strong shock wave hypothesis described previously. Values of impingement pressure predicted by Newtonian impact theory are also shown as a comparison over the entire length of the flat plate boundary.

Results of the present pressure analysis agree with the general conclusions drawn in References 1 and 2, based on experimental data for cold flow. For high values of h/R_e and low values of p_{t_e}/p_{AMB} (see Figures 9, 10 and 14 for hot flow, Figure 12 for cold flow) the peak pressure occurs at the point of impingement of the plume boundary on the plate, with another discontinuity occurring where the lip shock intersects the plate. For low values of h/R_e and high values of p_{t_e}/p_{AMB} (see Figure 11 for hot flow and

Figure 13 for cold flow), the peak pressure occurs in the weak shock region downstream of the impingement point.

The case of the S-IVB Retro Motor impinging on the Centaur Panel (see Figure 2) is more complicated to analyze. Although the panel is parallel to the S-IVB nozzle axis of symmetry, the panel curvature adds a new dimension of relief associated with the three-dimensional "spreading" effect of the impingement flow. Although the pressure distribution along the panel centerline shown in Figure 14 was predicted with a relieved boundary of the form given by Equation (1), the parameters a and $\tan\theta$ do not have the same relationships shown in Figures 6 and 7 for a flat plate. An interesting feature of this flow field is that the impingement shock wave lies approximately parallel to the panel centerline for a large portion of the distance downstream; this is a result of the additional amount of flow relief provided by the panel curvature and the fact that $\bar{h}$ is large. Hence, the good agreement of experimental pressure data with Newtonian impact theory.

The analytical pressure distributions shown along with test data for the S-IB Retro scale model test in Figure 15 and the S-II Retro scale model test in Figure 18 do not make use of the flat plate theory and Equation (1) for the relieved boundary of the impingement flow field. In the case of the S-IB, the exhaust plume impinged on a blast deflector ramp and then a curved interstage panel which was angled away from the nozzle axis of symmetry. The configuration of the S-II Retro was similar to the S-IB Retro, with the addition of one more expansion corner. Although no general theory has been postulated to handle the more complex flow fields such as the S-IB Retro, a fictitious upper boundary for an axisymmetric method-of-characteristics impingement flow field was used to predict the pressure distribution. Since two shock waves are created in this flow field (see Figure 16), it was necessary to generate the impingement flow field in two separate runs which had different altered boundaries; the first flow field used a straight line boundary canted at an angle of five degrees away from the physical boundary at the supersonic turning point, while the second flow field used a straight line boundary canted ten degrees away from the physical boundary at the compression corner responsible for the second shock wave. The S-II Retro impingement flow field was created in an analogous manner. Evidence that the S-IB Retro flow field, including placement of shock waves, is close to the actual flow field is provided by a comparison of total pressure calculated from the method-of-characteristics to the experimental values measured by a total pressure rake in the flow field as shown in Figure 17.

A particularly interesting phenomenon can be observed from the experimental data for both of these cases. A secondary peak in the data (see Figures 15 and 18 for pressure, Figure 22 for S-IB heat transfer) is very much in evidence at a downstream location of $x \cong 5.0$ inches and is not predicted by the theoretical impingement flow fields. The curved interstage panel under impingement was constructed with evenly spaced stringers which remain a constant height above the interstage surface of skin, i.e., identical to flight configurations. The three-dimensional spreading effect of the flow over the curved interstage panel creates secondary impingement shock waves from the two stringers adjacent to the centerline stringer. The rise in experimental heat transfer and pressure data is due to these secondary impingement shocks from the adjacent stringers crossing the top of the centerline stringer where the measurements were being taken.

5.2 HEAT TRANSFER RATE

Analytical heat transfer rates and experimental data are compared for three cases typical of the flat plate results in Figures 19, 20 and 21. The results indicate that turbulent boundary layer heat transfer theory correlates the experimental data much better than laminar boundary layer theory. For the cases analyzed, the general trend is for the NAA laminar [Equation (21)] curve to be the lowest, followed by the Blasius laminar and the iteration laminar methods which predict slightly higher values. It appears that the method based on the Spalding and Chi turbulent skin friction hypothesis matches the experimental data more closely than any turbulent method, a fact that Wallace (Reference 51) also observed in his analysis of hypersonic turbulent boundary layers in rocket nozzles and on a flat plate. In several cases, however, the turbulent Blasius method also predicts values of heat transfer which are close to the data. The Blasius method incorporated the accurate determination of reference quantities associated with the iteration procedure.

The method used to predict heat transfer rates in the strong shock region for the flat plate cases is based on a modified Fay and Riddell stagnation point heating equation. It does not appear to be as reliable as the weak shock region methods. A method for predicting strong shock region heating rates due to Africano (Reference 13) is also shown on the graphs for comparison. A great number of experimental data points in this narrow region would help in deriving and confirming a more detailed theory. The presence of data points to the left of the axial position at which the undisturbed plume free boundary intersects the plate would indicate that flow reversal did indeed take place. Since these two models have neglected the viscous flow reversal problem, accurate predictions of heat transfer in the strong shock region would not be expected.

The predicted heat transfer rates for the S-IB retro are shown against the experimental data in Figure 22. Also included on the figure at $x_e = 3.2$ inches are the AS-201 and AS-202 flight data points which were multiplied by the turbulent scale factor $(\ell_{FS}/\ell_M)^{0.2} = 1.585$ since the model lengths were 1/10 of the full-scale vehicle. The flight data points agree well with the theoretical heat transfer rates. As has been pointed out earlier, the comparison between theory and experimental data beyond $x_e \cong 4.0$ is clouded by the fact that the secondary impingement shock waves from the adjacent stringers cross the centerline stringer.

The comparison between theoretical and experimental heat transfer heat rates due to the exhaust of the S-IVB Retro is shown in Figure 23. Even though the pressure distribution was accurately predicted, it appears that the theoretical boundary layer methods have predicted values of heat transfer rate which are low in comparison to the data. This illustrates an important point concerning application to impingement problems on curved panels. Throughout the present analysis, the boundary layer-heat transfer phenomenon along the centerline of the impinged surface has been treated as locally two-dimensional. Although this assumption closely approximates impingement flow on a flat plate surface, it does not account for the additional relief mechanism affecting the boundary layer on a curved panel. The spanwise pressure gradients along the centerline are more pronounced for this case. Hence, the corresponding cross flow will reduce the boundary layer thickness compared to a two-dimensional calculation. The heat transferred to the surface will be greater for a "thinner" boundary layer. Future predictions of heat transfer rate on curved panels due to rocket exhaust plume impingement may require a three-dimensional boundary layer analysis to correctly simulate the physical problem.

Section 6
CONCLUSIONS

Methods have been developed for predicting pressures and heat transfer rates resulting from rocket nozzle exhaust plumes impinging on flat plates and curved panels. For the case of a flat plate parallel to the nozzle axis of symmetry, a technique of predicting centerline pressure from an axisymmetric method-of-characteristics impingement flow field with a relieved upper boundary specified by a cubic equation was found to give good agreement with both cold and hot gas experimental data. In the strong shock region pressure distributions were found from a linear interpolation formula based on the shock angle and turning angle for strong, maximum strength weak, and normal shock waves. Impingement pressure peaks were found to occur at the theoretical impingement point of the plume boundary on the plate for high values of h/R_e and low values of p_{t_e}/p_{AMB} and to occur further downstream when the conditions were reversed. Three-dimensional flow relief effects on the centerline of curved panels canted away from the nozzle axis of symmetry were also simulated using the technique of altering the axisymmetric flow field boundary which provides a close agreement with experimental pressure data.

Heat transfer calculations in the weak shock region, based on the Spalding and Chi turbulent skin friction relation, agreed quite closely with experimental data. The good agreement between heating rates based on the Spalding and Chi turbulent skin friction law and experiment would imply that the original Spalding and Chi hypothesis, derived on the basis of a zero pressure gradient flow, continues to be valid in the presence of a pressure gradient.

Future plans call for investigation of rarefied flow effects (at higher altitudes) and for prediction of pressures and heating rates off the centerline of flat plates and curved panels. In summary, it is felt that the current methods of predicting pressure and heating caused by rocket exhaust impingement provide an improvement over previous methods of analysis for all of the test data analyzed.

Section 7

REFERENCES

1. Bauer, R. C. and R. L. Schlumpf, "Experimental Investigation of Free Jet Impingement on a Flat Plate," TN-60-223, Arnold Engineering Development Center, Tullahoma, Tenn., March 1961.

2. Vick, A. R. and E. H. Andrews, "An Experimental Investigation of Highly Underexpanded Free Jets Impinging Upon a Parallel Flat Surface," TN D-2326, NASA/Langley, Hampton, Va., June 1964.

3. Margolin, E. L. and E. Welch, "Final Report – Single Nozzle Jet Plume Test in the Rocket Nozzle Test Facility," SID 63-426, North American Aviation, Downey, Calif., May 1963.

4. Gopin, A. J. and E. L. Margolin, "A Cold Gas, Short-Duration Technique for High Altitude, Underexpanded Jet Exhaust Impingement Studies," SID 64-1639, North American Aviation, Downey, Calif., September 1964.

5. "Research on Base Heating of Rocket Motor Vehicles Using Shock Tube Techniques," Cornell Aeronautical Laboratory Progress Report No. 43 (Project No. HM-1510-Y) under Contract NAS8-823, Cornell Aeronautical Laboratory, Buffalo, New York, June 1964.

6. Runyan, R. B., "Rocket Plume Investigation at Pressure Altitudes Above 175,000 Feet," TDR-63-180, Arnold Engineering Development Center, Tullahoma, Tenn., September 1963 (CONFIDENTIAL).

7. Barebo, R. L. and R. C. Ansley, "Effects of Rocket Exhaust Jet Impingement on a Movable Flat Plate at Pressure Altitude Above 200,000 Feet," TDR-63-214, Arnold Engineering Development Center, Tullahoma, Tenn., January 1964 (CONFIDENTIAL).

8. Piesik, E. T. and M. L. Lofland, "High-Vacuum Plume Impingement Test Report," SID 63-1520, North American Aviation, Downey, Calif., February 1964.

9. Boudreax, R. A. and F. G. Etheridge, "Attitude Control Rocket Exhaust Plume Experimental Final Report – Phases 1 and 2," TR-67-3, Air Force Rocket Propulsion Laboratory, Air Force Systems Command, Edwards, Calif., February 1967.

10. Lehrer, S., "Investigation of Spacecraft Rocket Installation Areas – Vehicle Heating," TR-64-141 Vol. II, Air Force Rocket Propulsion Laboratory, Air Force Systems Command, Edwards, Calif., November 1964.

11. Piesik, E. T., "High-Vacuum Plume Impingement Test Correlation," SID 64-1563, North American Aviation, Downey, Calif., August 1964.

12. Piesik, E. T., R. R. Koppang and D. J. Simkin, "Rocket-Exhaust Impingement on a Flat Plate at High Vacuum," AIAA Journal of Spacecraft and Rockets, Vol. 3, No. 11, pp. 1650 - 1657, November 1966.

13. Africano, A., "Engineering Method to Predict Saturn V Vehicle and Launch Complex Environments Due to Rocket Jet Impingement," SID 65-816, North American Aviation, Downey, Calif., July 1965.

14. Lewis, C. H., R. D. Hackett and W. C. Kuby, "Effects of Impingement of Rocket Exhaust Gases and Solid Particles," Interim Report under Jet Propulsion Laboratory Contract 951246, Philco-Ford Corp., Aeronutronic Div., Newport Beach, Calif., November 1966.

15. Rochelle, W. C., "Summary of Heat Flux and Pressure Instrumentation Used in Recent Saturn Rocket Exhaust Tests," TM X-53613, NASA/Marshall Space Flight Center, Huntsville, Ala., May 1967.

16. Rochelle, W. C., "Theoretical and Experimental Investigation of Heating from Saturn Solid Propellant Rocket Exhausts," AIAA Paper 66-653, June 1966, presented at AIAA Second Propulsion Joint Specialist Conference, June 13 - 17, 1966.

17. Rochelle, W. C., "Analyses of Heating Rates Along S-IB/S-IVB Aft Interstage Due to Retrorocket Exhaust Impingement — Design Criteria for Vehicle 201," Memorandum R-AERO-AT-65-30, NASA/Marshall Space Flight Center, Huntsville, Ala., October 1965.

18. Gibson, J. G., "S-IB/S-IVB Interstage Convective Heating Due to Impingement of S-IB Retro-Motor Exhaust Plume," LMSC/HREC A712665, Lockheed Missiles & Space Company, Huntsville, Ala., December 1965.

19. Rochelle, W. C., "S-IC/S-II Interstage and S-IC Forward Skirt Pressure Environment Due to Rocketdyne RS-U-501 S-II Ullage Motor Exhaust Impingement," Memorandum R-AERO-AT-66-3, NASA/Marshall Space Flight Center, Huntsville, Ala., June 1966.

20. Rochelle, W. C., "Experimental Determination of Heating Rates and Impingement Pressures from Centaur Retrorocket Exhausts," Memorandum R-AERO-AT-66-4, NASA/Marshall Space Flight Center, Huntsville, Ala., June 1966.

21. Gardon, R., "An Instrument for the Direct Measurement of Intense Thermal Radiation," Review of Scientific Instruments, Vol. 24, No. 25, pp. 360 - 370, May 1963.

22. Muse, W. W., "Full-Scale Simulated Altitude Investigation of the Centaur-Payload Surface and Functional Degradation Resulting from the Saturn S-IVB Retro Rocket Exhaust Contaminants," TR-66-57, Arnold Engineering Development Center, Tullahoma, Tenn., May 1966.

23. Rochelle, W.C., "Preliminary Test Plan for Retrorocket Tests at Cornell Aeronautical Laboratory," Memorandum R-AERO-AT-65-29, NASA/ Marshall Space Flight Center, Huntsville, Ala., October 1965.

24. Dennis, R. J. and Hendershot, K. C., "Research on Base Heating of Rocket Motor Vehicles Using Shock Tube Techniques," Cornell Aeronautical Laboratory Progress Reports 17-26 (Project No. HM-2045-Y) under Contract NAS8-20027, Cornell Aeronautical Laboratory, Buffalo, New York, June 1966 to March 1967.

25. Hendershot, K.C., "The Application of Short-Duration Techniques to the Experimental Study of Base Heating," HM-1510-Y-18, Cornell Aeronautical Laboratory, Buffalo, New York, April 1965.

26. Martin, J.F., G.R. Duryea and L.M. Stevenson, "Instrumentation for Force and Pressure Measurements in a Hypersonic Shock Tunnel," 113, Cornell Aeronautical Laboratory, Buffalo, New York, January 1962.

27. Bogden, L., "High-Temperature, Thin-Film Resistance Thermometers for Heat Transfer Measurement," HM-1510-Y-6, Cornell Aeronautical Laboratory, Buffalo, New York, February 1963.

28. Hendershot, K.C., "Research on Base Heating of Rocket Motor Vehicles Using Shock Tube Techniques," Cornell Aeronautical Laboratory Progress Report No. 46 (Project No. HM-1510-Y) under Contract No. NAS8-823, Cornell Aeronautical Laboratory, Buffalo, New York, September 1964.

29. Usher, H., "S-I-3 Retrorocket (2 ks - 36250) Jet Heating Rates as Estimated from Thermocouple Data," Memorandum M-P&VE-PH-50-63, NASA/ Marshall Space Flight Center, Huntsville, Ala., March 1963.

30. Prozan, R. J., "Development of a Method of Characteristics Solution for Supersonic Flow of an Ideal, Frozen or Equilibrium Reacting Gas Mixture," LMSC/HREC A782535, Lockheed Missiles & Space Company, Huntsville, Ala., April 1966.

31. Farmer, R.C., R.J. Prozan, L.R. McGimsey and A.W. Ratliff, "Verification of a Mathematical Model which Represents Large, Liquid Rocket-Engine Exhaust Plumes," AIAA Paper 66-650, June 1966, presented at Second Propulsion Joint Specialist Conference, June 13 - 17, 1966.

32. D.Attorre, L., G. Nowak and H.U. Thommen, "Inviscid Analysis of the Plume Created by Multiple Rocket Engines," DBE-66-014, General Dynamics/Convair, San Diego, Calif., May 1966.

33. Lax, D.D. and B. Wendroff, "Difference Schemes with High Order of Accuracy for Solving Hyperbolic Equations," NYO-9759, New York University, New York, N.Y., July 1962.

34. Richtmeyer, R. D., "A Survey of Difference Methods for Non-Steady Fluid Dynamics," 63-2, National Center for Atmospheric Research, Boulder, Colorado.

35. Dorrance, W. H., Viscous Hypersonic Flow, First Ed., McGraw-Hill, New York, Chapters 4, 5 and 8, 1962.

36. Rosner, D. E., "Convective Heat Transfer with Chemical Reaction," ARL-99, Part I, Aeronautical Research Laboratory, Wright-Patterson Air Force Base, Dayton, Ohio, August 1961.

37. Goulard, R. J., "On Catalytic Recombination Rates in Hypersonic Stagnation Heat Transfer," Jet Propulsion, Vol. 28, pp. 737-745, 1958.

38. Bartz, D. R., "Turbulent Boundary Layer Heat Transfer from Rapidly Accelerating Flow of Rocket Combustion Gases and of Heated Air," Advances in Heat Transfer, Vol. 2, Academic Press, New York, pp. 1 - 108, 1960.

39. Hoenig, R. J., "LMSC/HREC Boundary Layer Computer Program — Theory," LMSC/HREC A782405, Lockheed Missiles & Space Company, Huntsville, Ala., March 1967.

40. Eckert, E. R. G., "Survey on Heat Transfer at High Speeds," ARL 189, Aeronautical Research Laboratory, Wright-Patterson Air Force Base, Dayton, Ohio, December 1961.

41. Svehla, R. A., "Thermodynamic and Transport Properties for the Hydrogen-Oxygen System," SP-3011, NASA, Washington, D. C., 1964.

42. Van Driest, E. R., "Investigation of Laminar Boundary Layer in Compressible Fluids Using the Crocco Method," TN-2597, NACA, Washington, D. C., 1952.

43. Clauser, F. H., "The Turbulent Boundary Layer," Advances in Applied Mechanics, Vol. 4, Academic Press, New York, pp. 1 - 52, 1956.

44. Danberg, J. E., "Characteristics of the Turbulent Boundary Layer with Heat and Mass Transfer at M = 6.7," TR-64-99, Naval Ordinance Laboratory, Washington, D. C., October 1964.

45. Shapiro, A. H., The Dynamics and Thermodynamics of Compressible Fluid Flow, Vol. 2, Ronald Press, New York, 1954.

46. Harkness, J. L., "Skin Friction and Heat Transfer Studies at Supersonic Speeds for Turbulent Boundary Layers," DRL-435, Defense Research Laboratory, University of Texas, Austin, Texas, January 1959.

47. Spalding, D. B. and S. W. Chi, "The Drag of a Compressible Turbulent Boundary Layer on a Smooth Flat Plate With and Without Heat Transfer," J. Fluid Mechanics, Vol. 18, Part 1, pp. 117 - 143, January 1964.

48. Spalding, D. B., "A New Analytical Expression for the Drag of a Flat Plate Valid for Both the Turbulent and Laminar Regimes," International Journal of Heat and Mass Transfer, Vol. 5, pp. 1133 - 1138, 1962.

49. Fay, J. A. and F. R. Riddell, "Theory of Stagnation Point Heat Transfer in Dissociated Air," J. Aeron. Sci., Vol. 25, No. 2, pp. 73 - 85, February 1958.

50. Kemp, N. H. and F. R. Riddell, "Heat Transfer to Satellite Vehicles Reentering the Atmosphere," Jet Propulsion, Vol. 27, No. 2, pp. 132 - 137, February 1957.

51. Wallace, J. E., "Hypersonic Turbulent Boundary Layer Studies at Cold Wall Conditions," Proceedings of the 1967 Heat Transfer and Fluid Mechanics Institute, Stanford University Press, pp. 427 - 451, 1967.

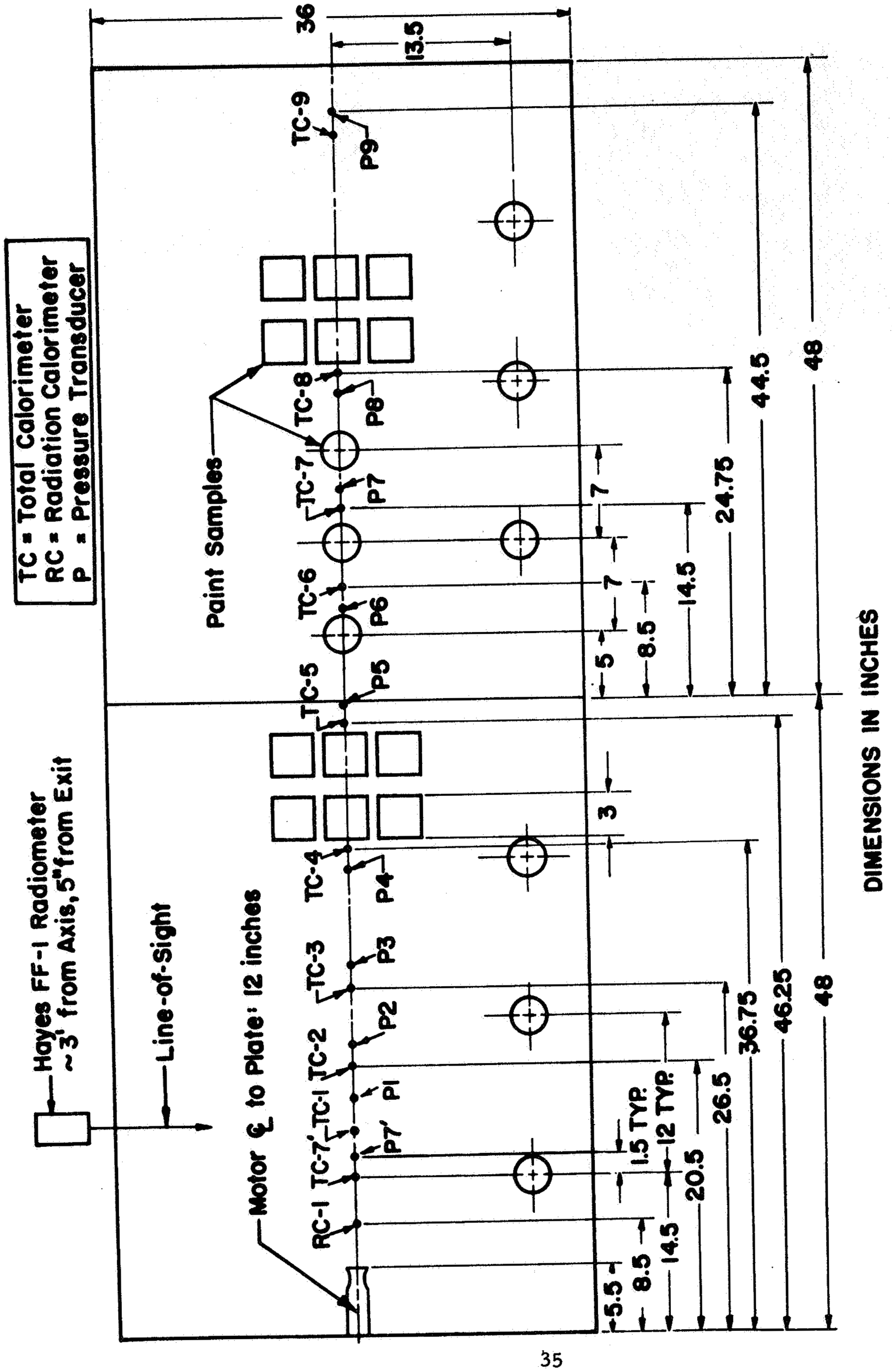
TC = Total Calorimeter
RC = Radiation Calorimeter
P = Pressure Transducer
Hayes FF-1 Radiometer
~3' from Axis, 5" from Exit
Line-of-Sight
Motor ℄ to Plate: 12 inches
Paint Samples
RC-1
TC-1
TC-7'
P7'
TC-1
P1
TC-2
P2
TC-3
P3
TC-4
P4
TC-5
P5
TC-6
P6
TC-7
P7
TC-8
P8
TC-9
P9
36
13.5
48
44.5
24.75
14.5
7
7
8.5
5
3
48
46.25
36.75
26.5
20.5
14.5
8.5
5.5
1.5 TYP.
12 TYP.
DIMENSIONS IN INCHES

FIGURE I. LOCATION OF INSTRUMENTATION ON FLAT PLATE FOR CENTAUR RETRO TESTS

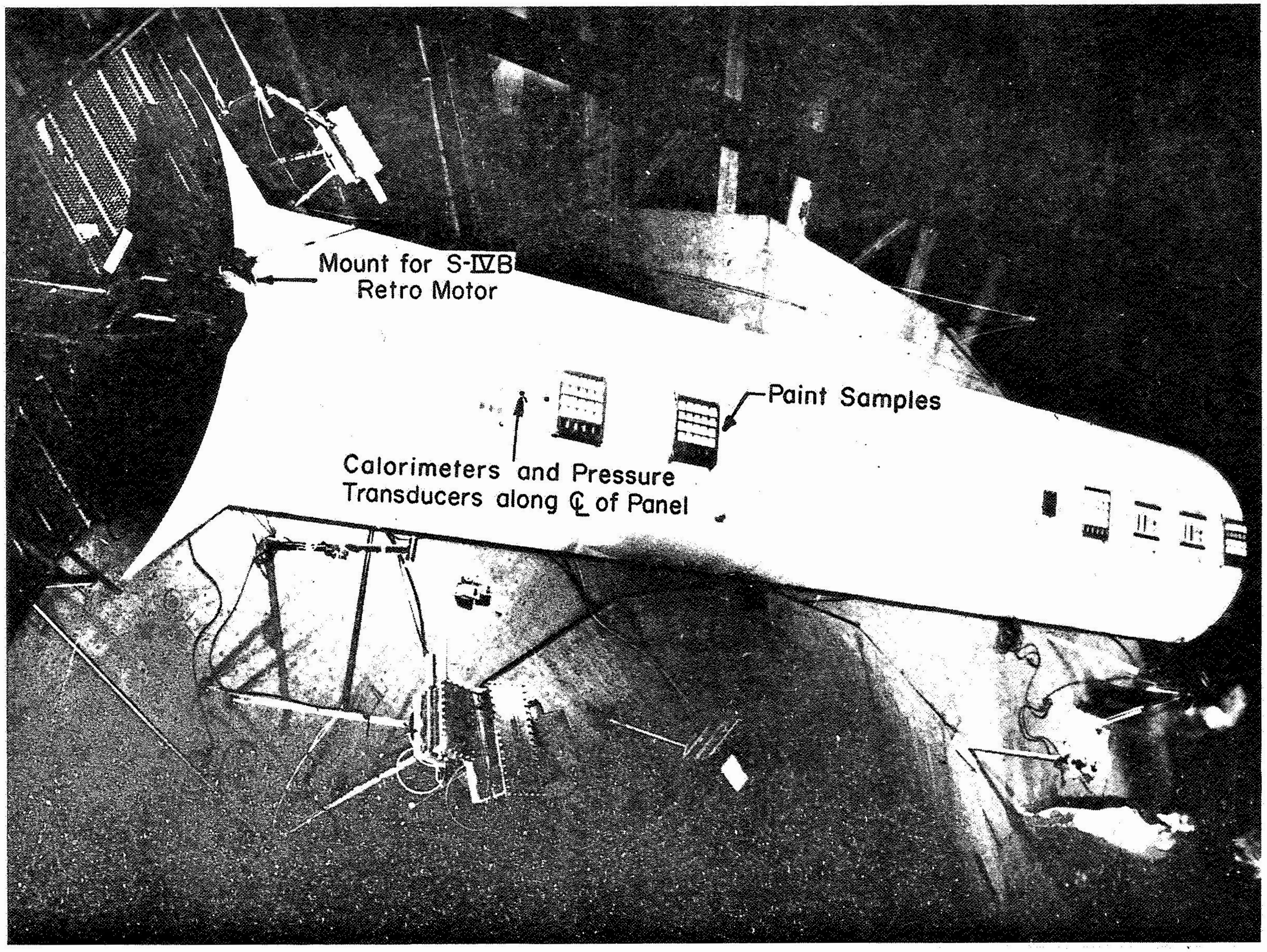
Mount for S-IVB
Retro Motor
Paint Samples
Calorimeters and Pressure
Transducers along ℄ of Panel

Figure 2 - Centaur Panel Used in S-IVB Retro Motor Tests

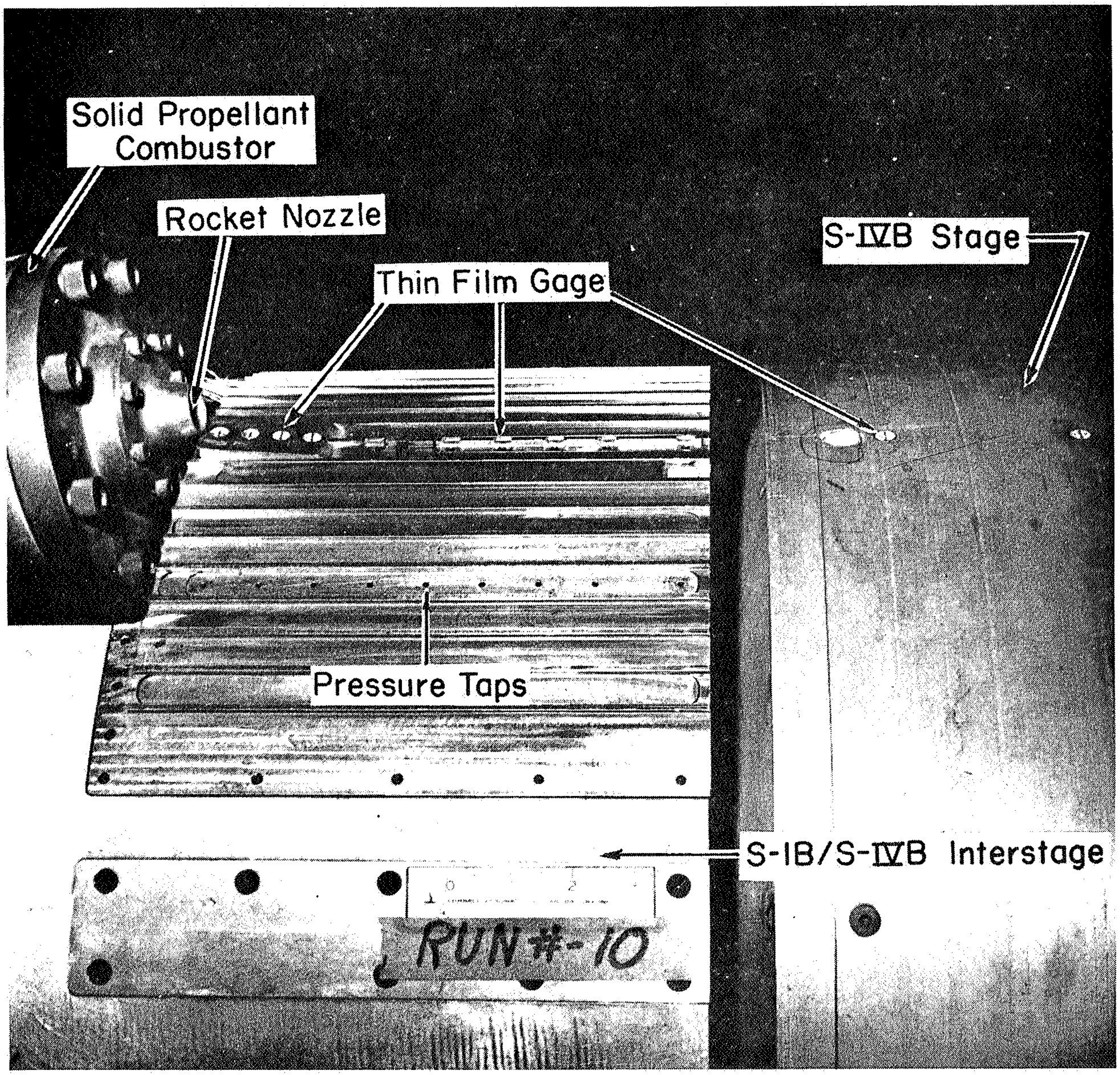
Solid Propellant Combustor
Rocket Nozzle
Thin Film Gage
S-IVB Stage
Pressure Taps
S-IB/S-IVB Interstage
RUN #-10

Figure 3 - S-IB/S-IVB Interstage Used in S-IB Retro Tests at CAL

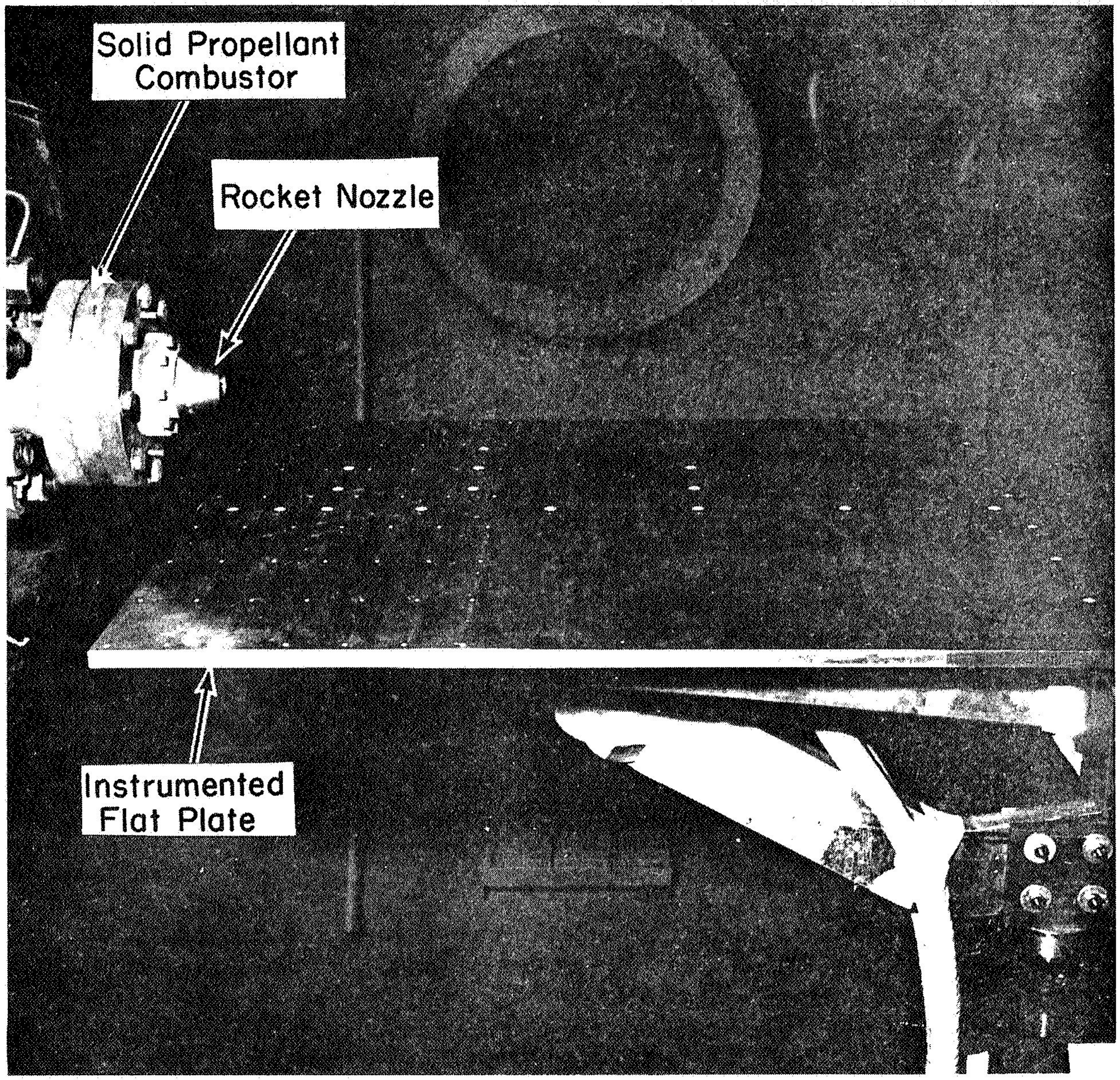
Solid Propellant Combustor
Rocket Nozzle
Instrumented Flat Plate

Figure 4 - Flat Plate Used in RDS-507 Propellant Tests at CAL

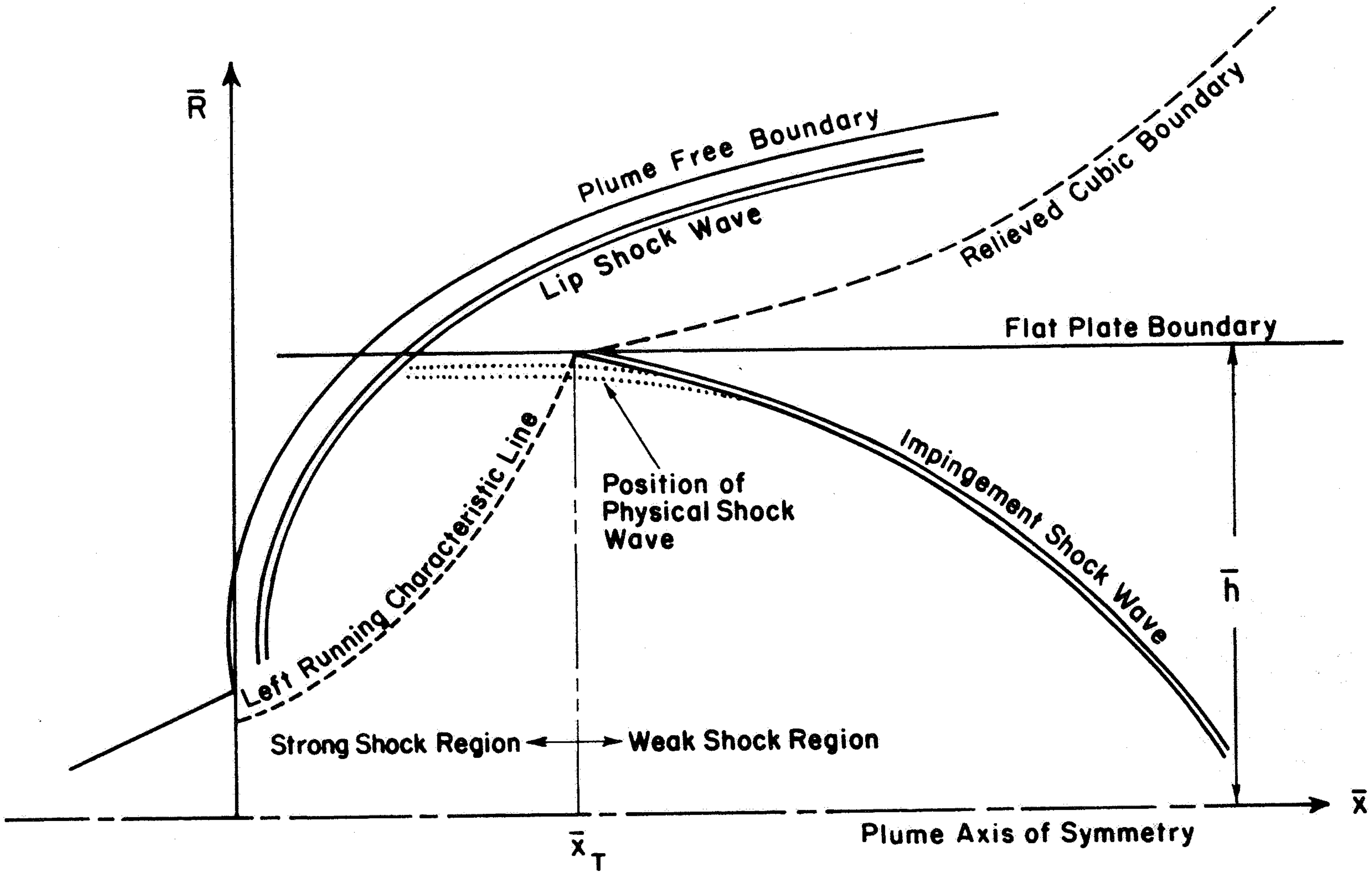
$\bar{R}$
Plume Free Boundary
Lip Shock Wave
Relieved Cubic Boundary
Flat Plate Boundary
Left Running Characteristic Line
Position of Physical Shock Wave
Impingement Shock Wave
$\bar{h}$
Strong Shock Region
Weak Shock Region
$\bar{x}$
$\bar{x}_T$
Plume Axis of Symmetry

FIGURE 5. DESCRIPTION OF FLAT PLATE IMPINGEMENT PROBLEM (NOT TO SCALE)

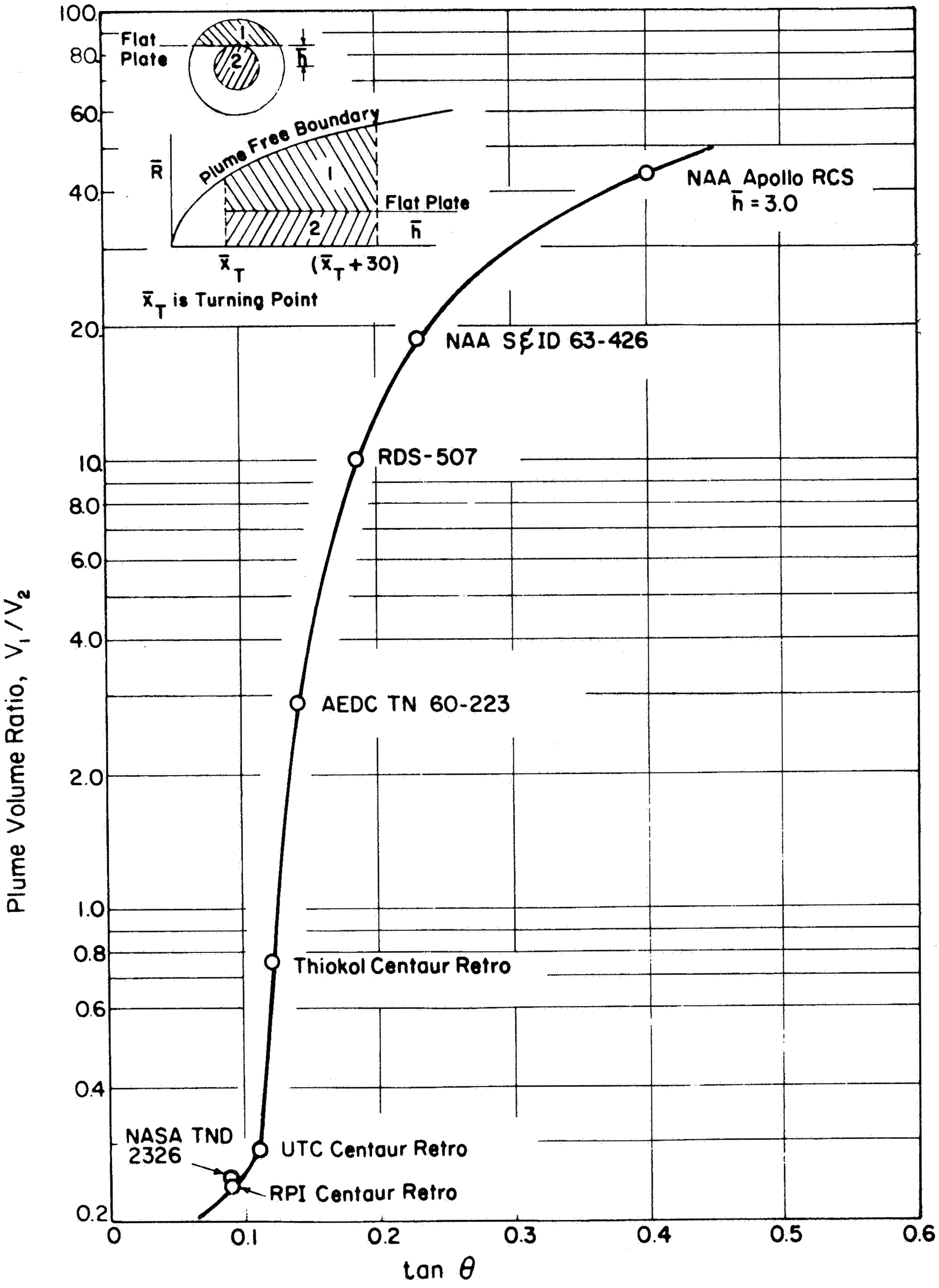

FIGURE 6. RELATIONSHIP BETWEEN PLUME VOLUME RATIO, V_1/V_2, AND PARAMETER, TAN θ

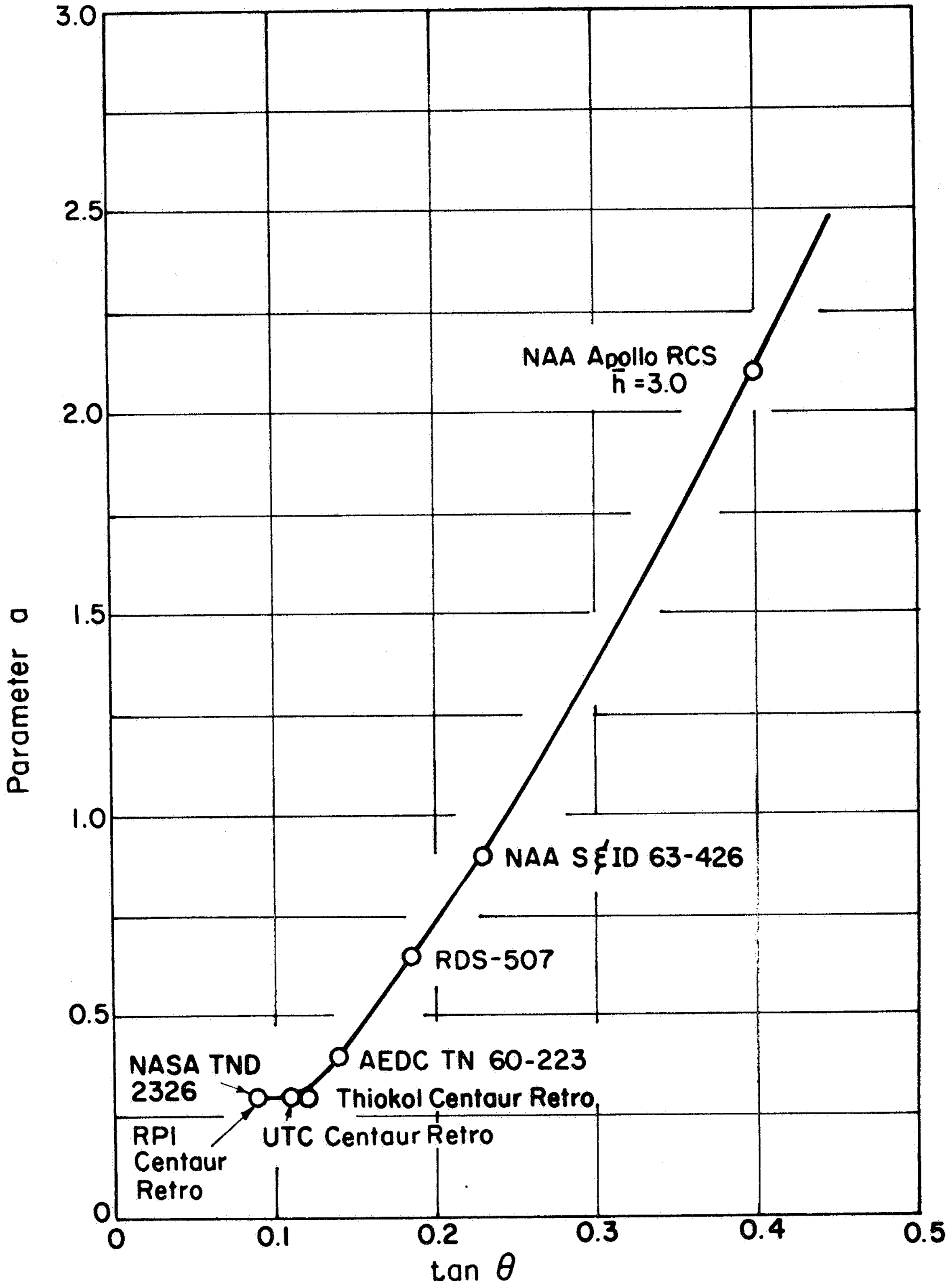

FIGURE 7. RELATIONSHIP BETWEEN PARAMETER a AND PARAMETER TAN θ

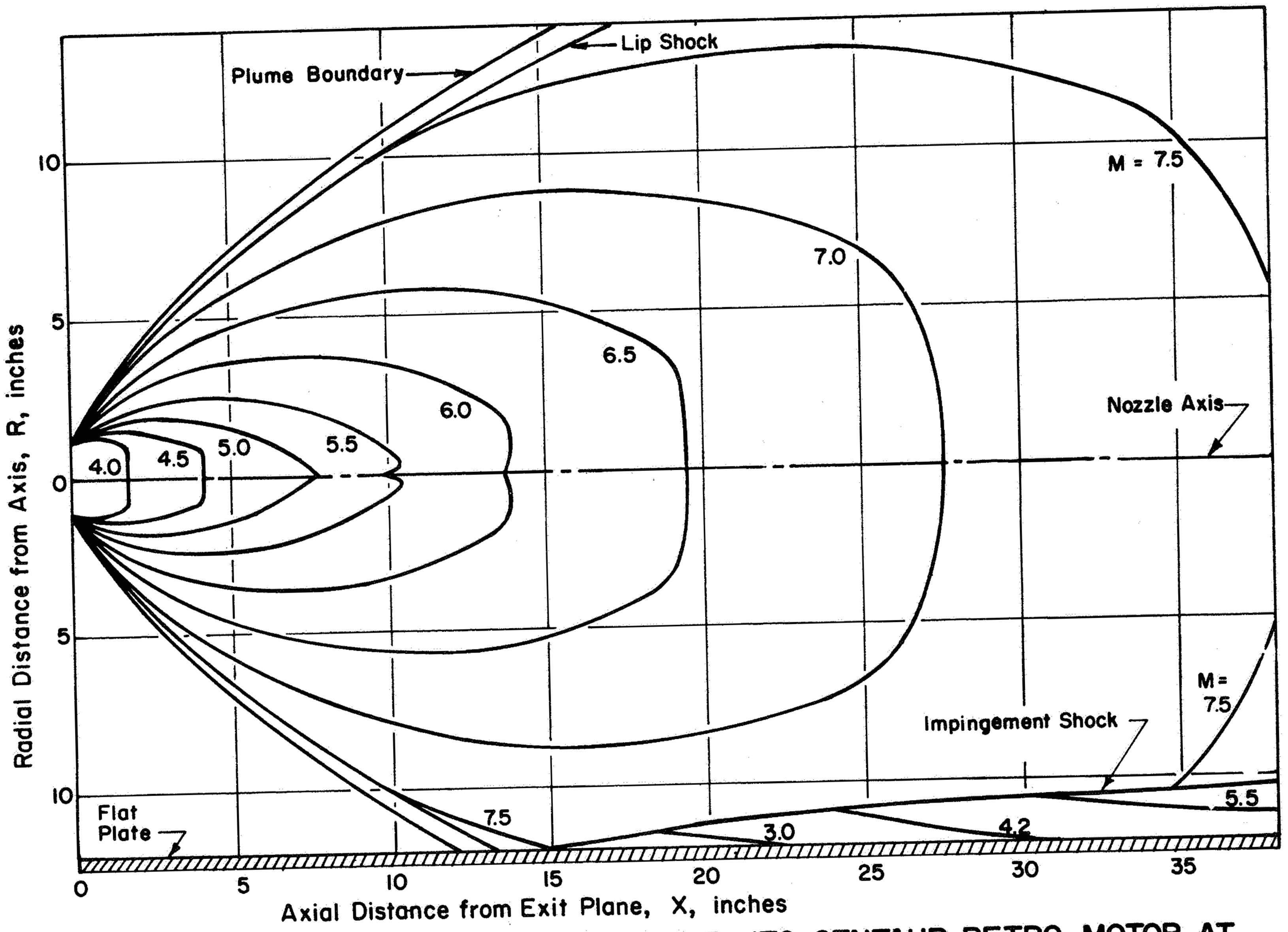

FIGURE 8. MACH NUMBER CONTOURS FOR UTC CENTAUR RETRO MOTOR AT 109,000 FEET

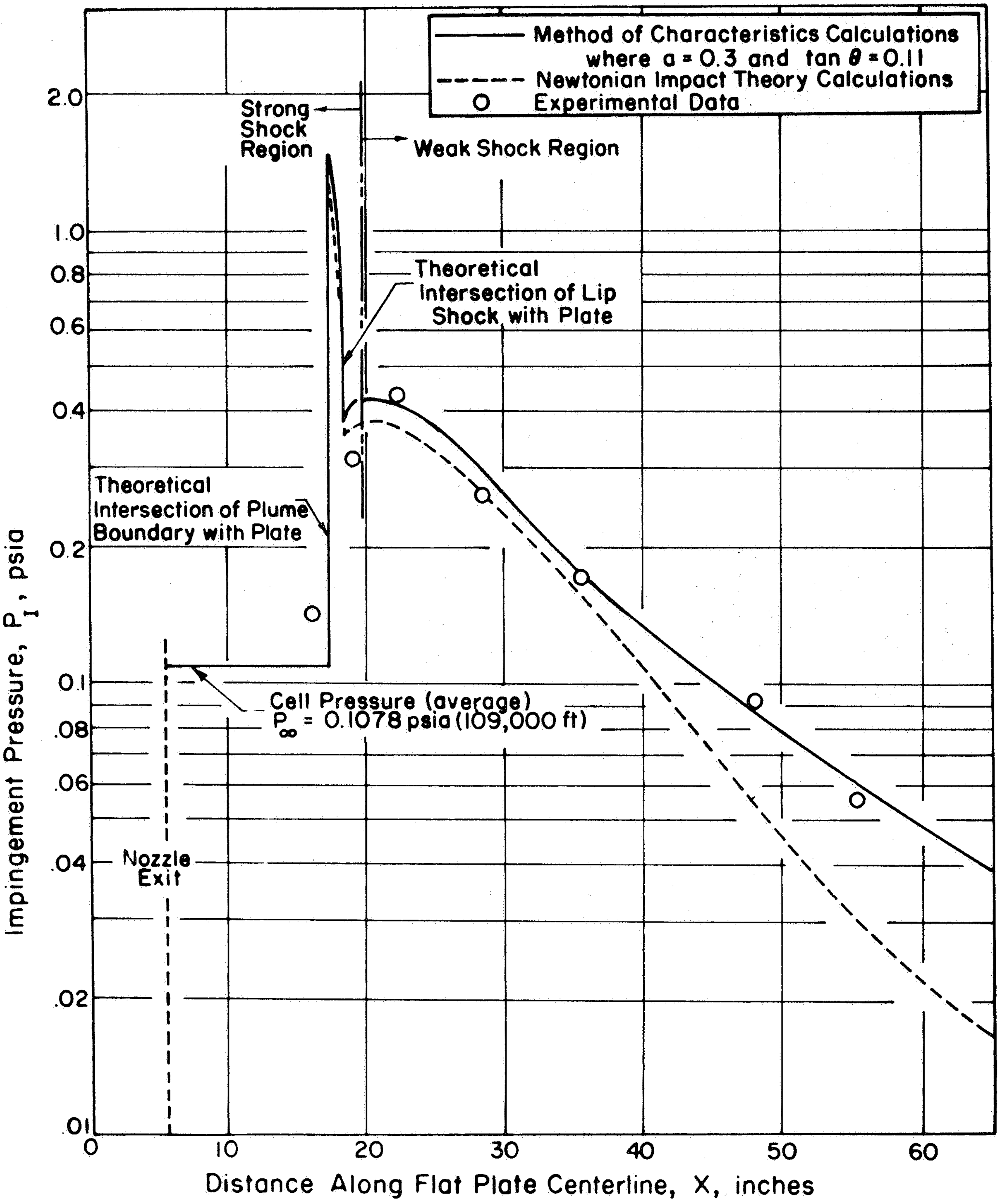

FIGURE 9. COMPARISON OF PRESSURES ON FLAT PLATE DUE TO EXHAUST OF UTC CENTAUR RETRO MOTOR AT 109,000 FEET

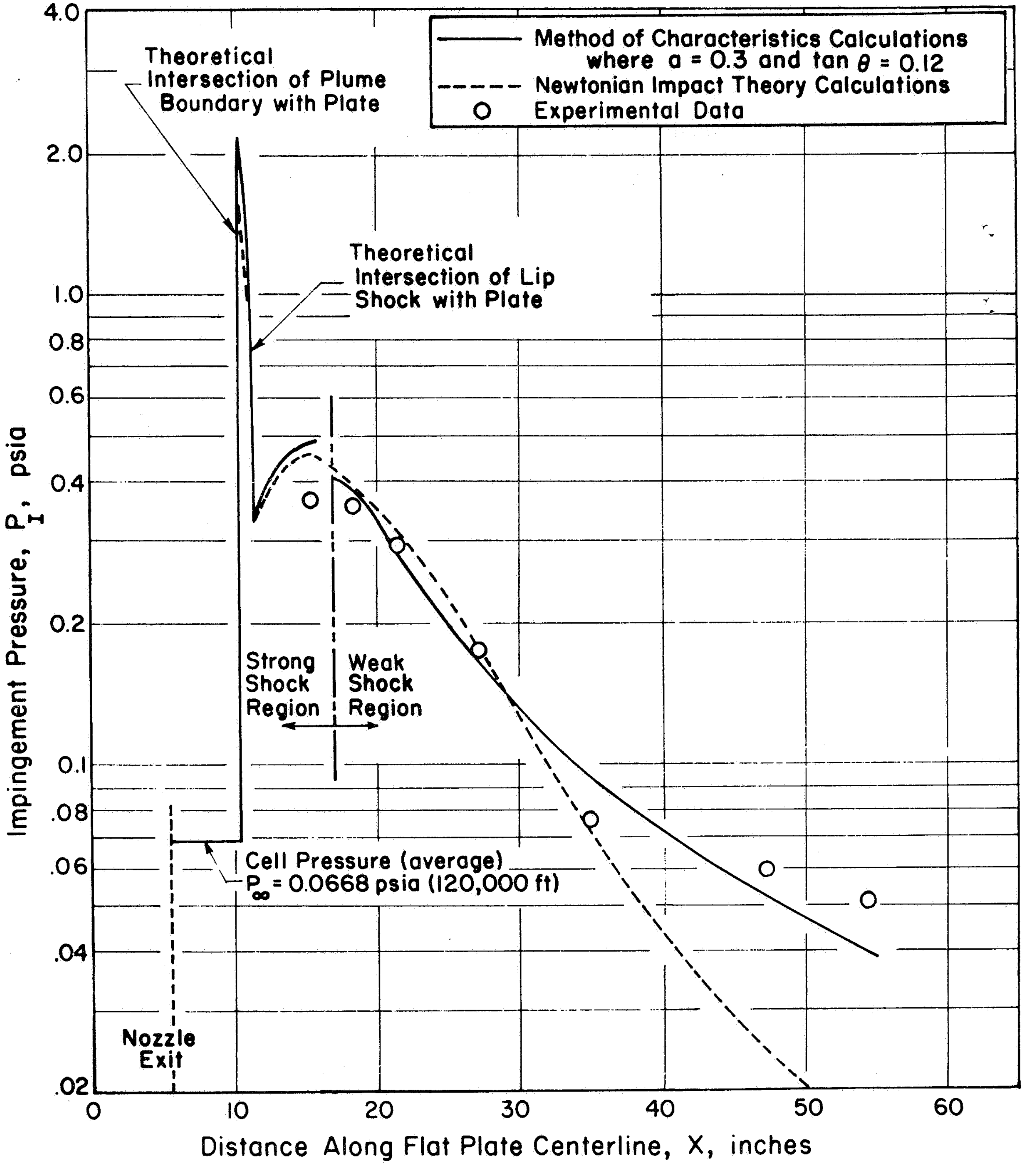

FIGURE 10. COMPARISON OF PRESSURES ON FLAT PLATE DUE TO EXHAUST OF THIOKOL CENTAUR RETRO MOTOR AT 120,000 FEET

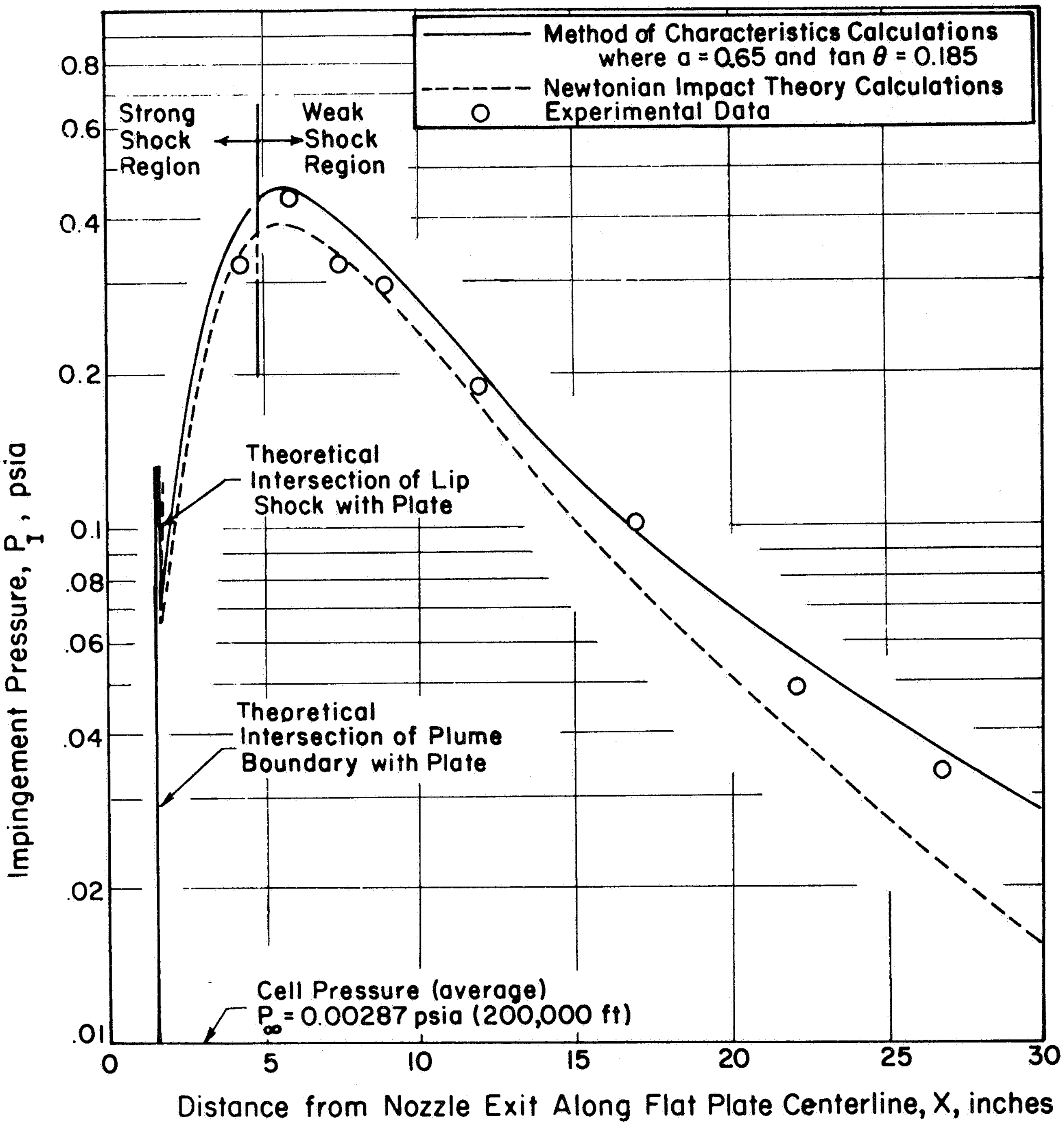

FIGURE 11. COMPARISON OF PRESSURES ON FLAT PLATE DUE TO EXHAUST OF RDS-507 MOTOR AT 200,000 FEET

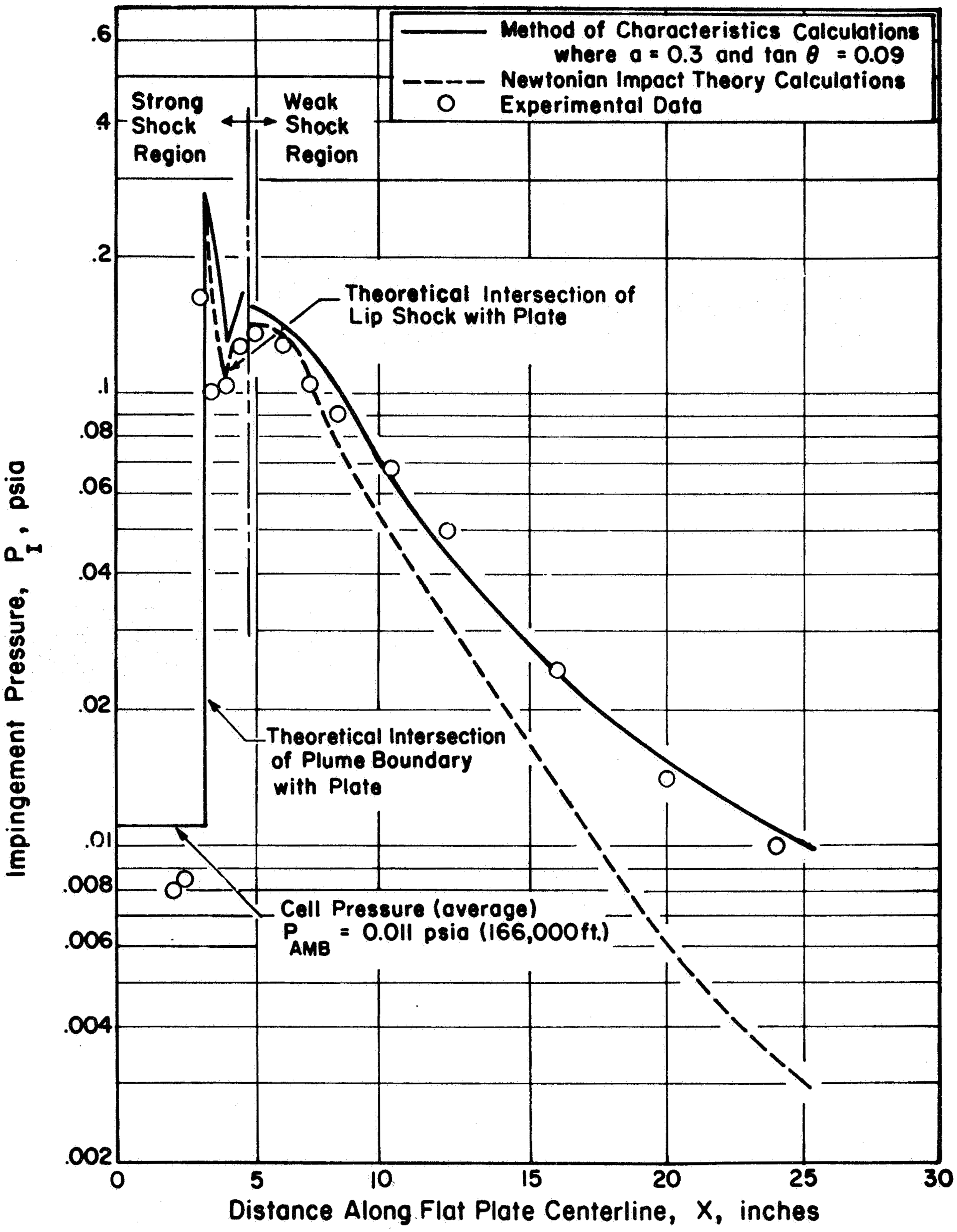

FIGURE 12. COMPARISON OF PRESSURES ON FLAT PLATE DUE TO EXHAUST OF AIR (FROM REFERENCE 2) AT 166,000 FEET

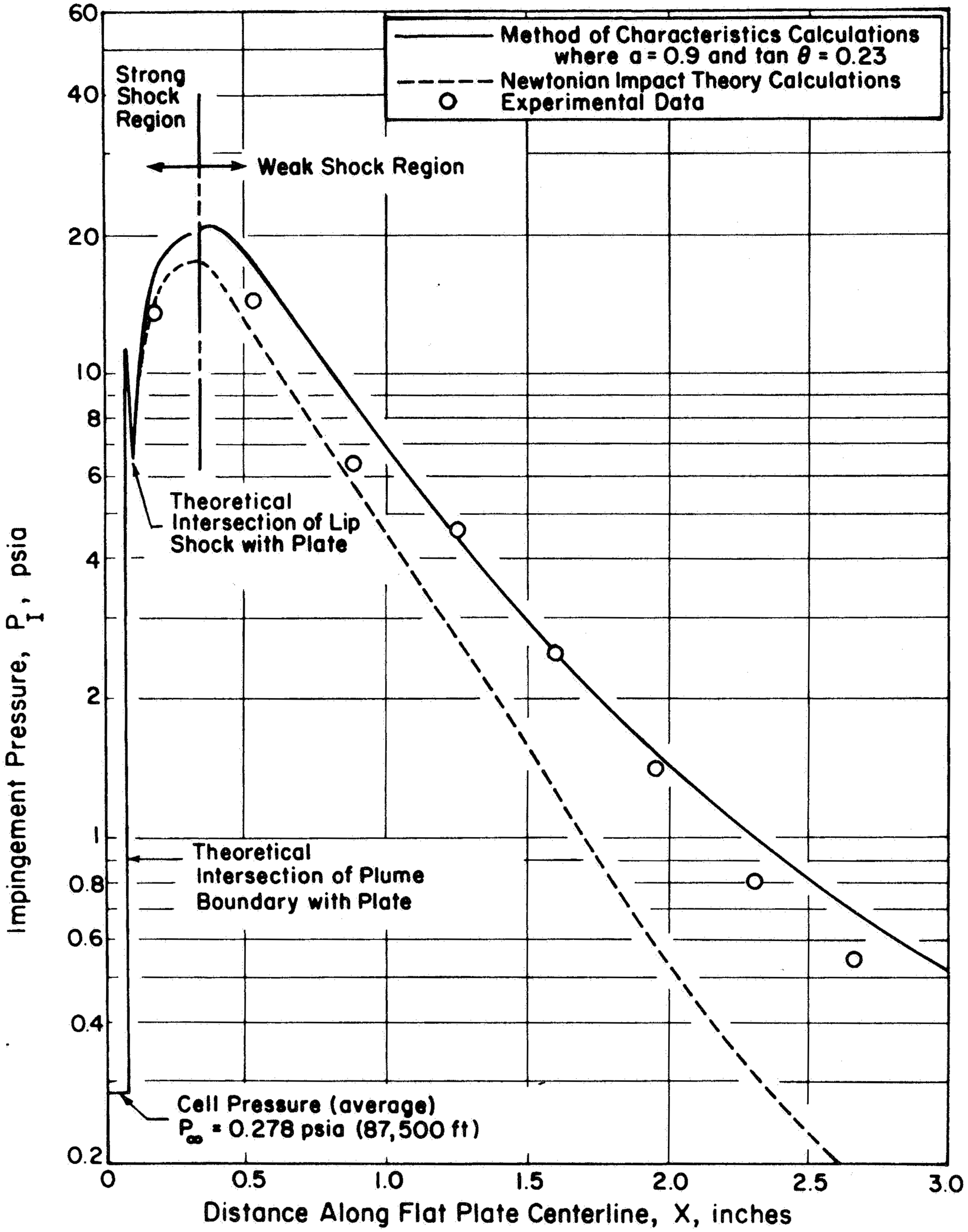

FIGURE 13. COMPARISON OF PRESSURES ON FLAT PLATE DUE TO EXHAUST OF NITROGEN (FROM REFERENCE 3) AT 87,500 FEET

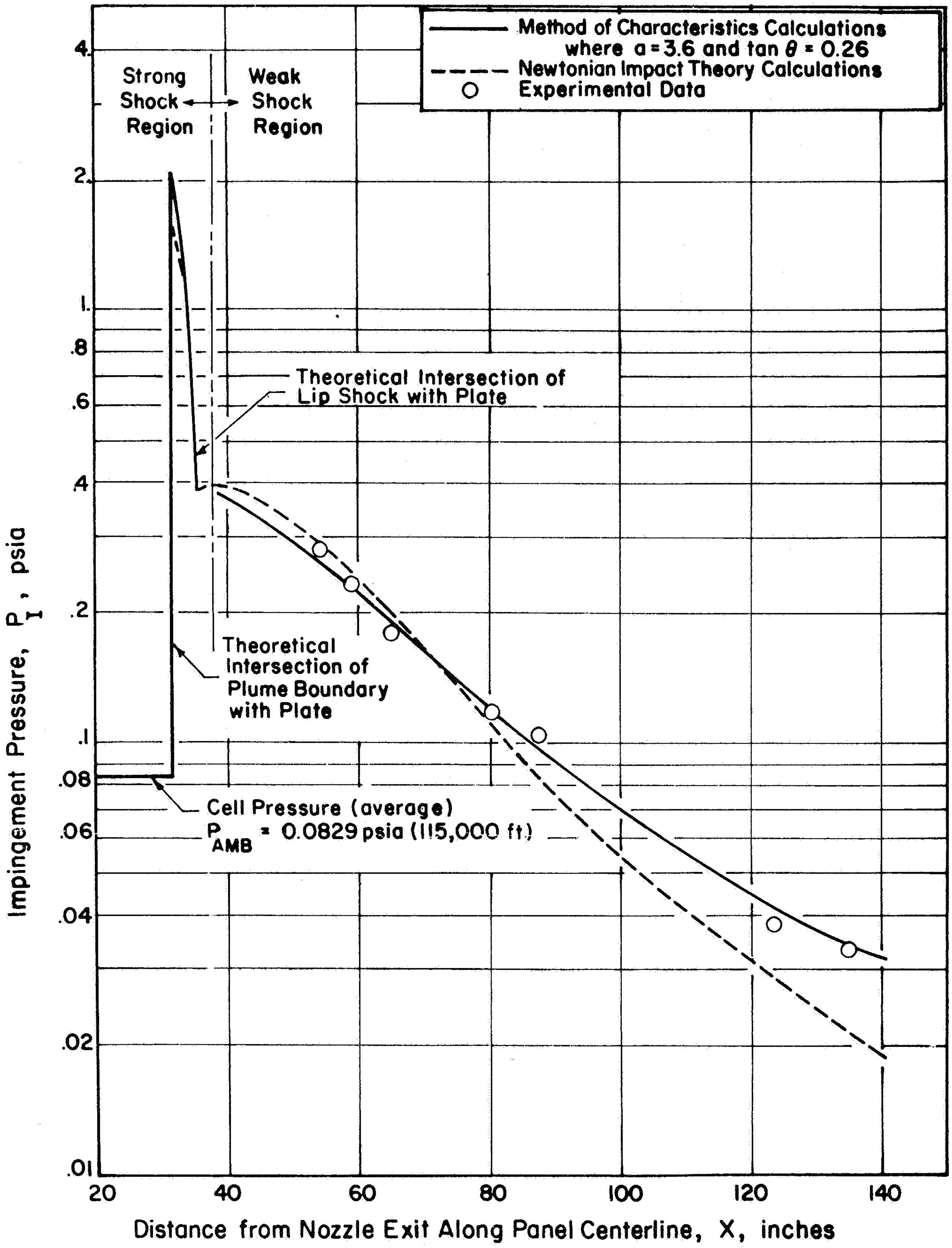

FIGURE 14. COMPARISON OF PRESSURES ON CENTAUR PANEL DUE TO EXHAUST OF S-IVB RETRO MOTOR AT 115,000 FEET

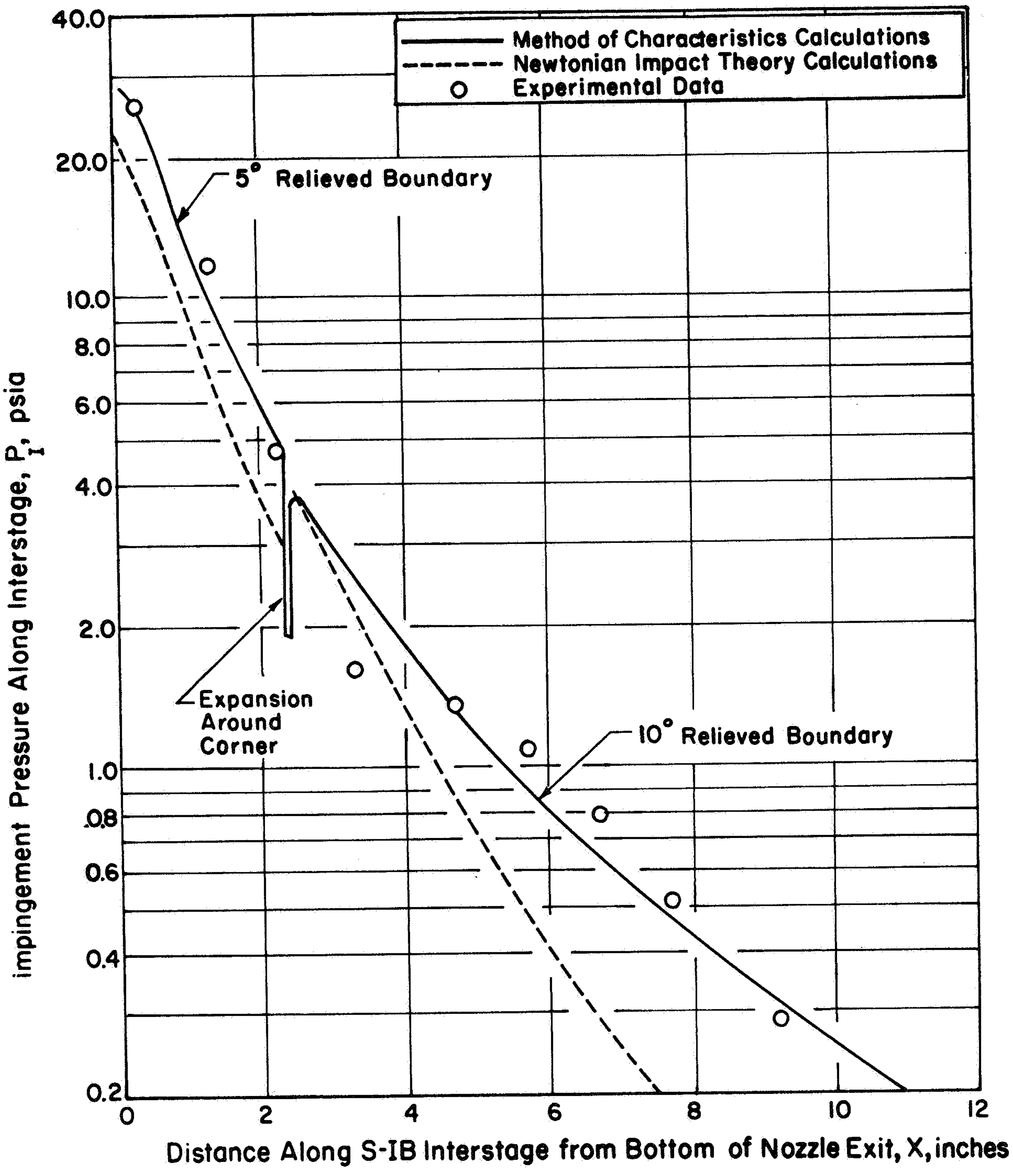

FIGURE 15. COMPARISON OF PRESSURES ON S-IB/S-IVB INTERSTAGE DUE TO EXHAUST OF S-IB RETRO MOTOR AT 200,000 FEET

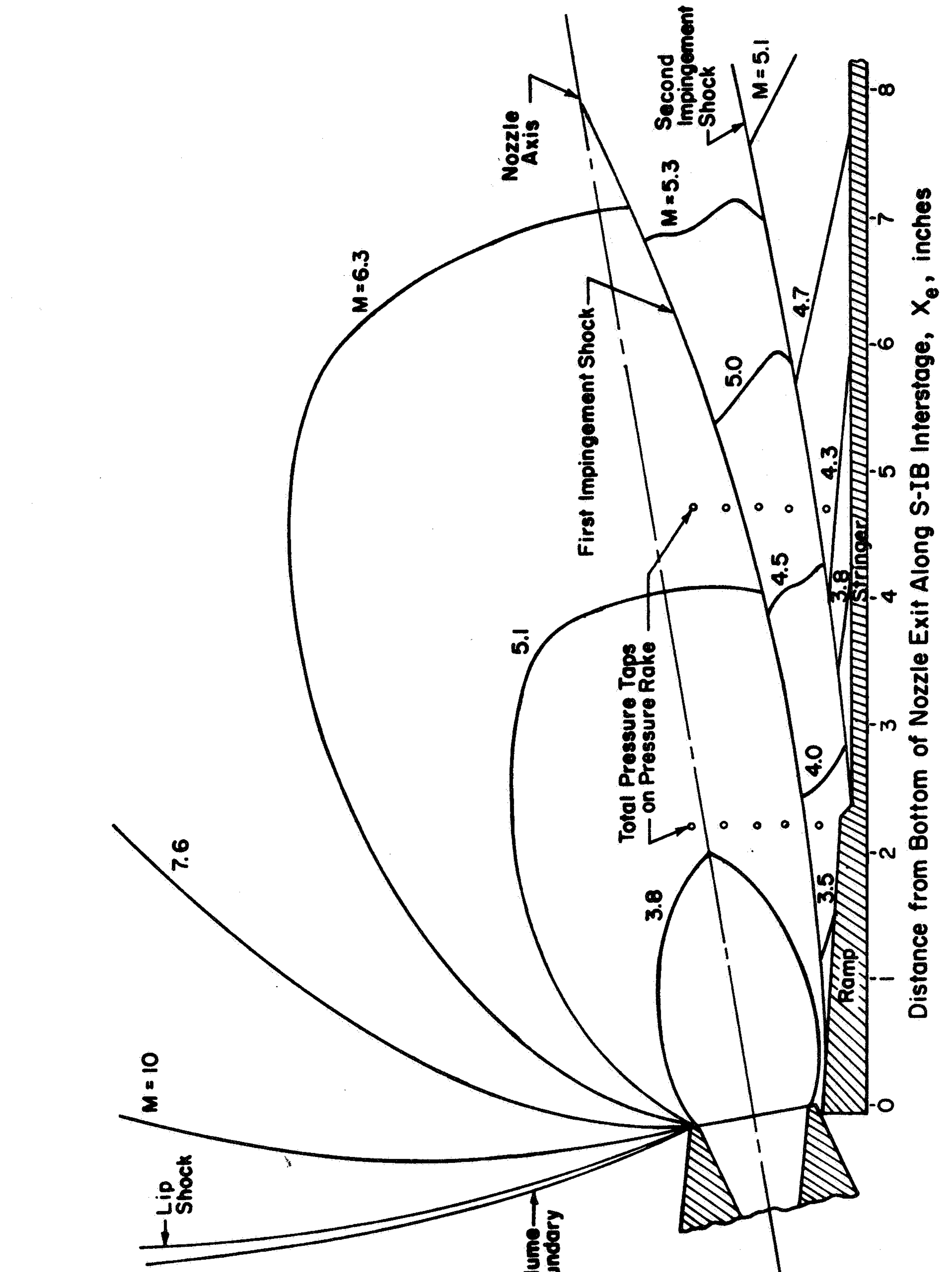
Lip Shock
Plume Boundary
M = 10
7.6
M = 6.3
5.1
3.8
3.5
Ramp
4.0
Total Pressure Taps on Pressure Rake
4.5
3.8
Stringer
4.3
First Impingement Shock
5.0
4.7
M = 5.3
Nozzle Axis
Second Impingement Shock
M = 5.1
0
1
2
3
4
5
6
7
8
Distance from Bottom of Nozzle Exit Along S-IB Interstage, X_e, inches

FIGURE 16. MACH NUMBER CONTOURS FOR S-IB RETRO MOTOR AT 200,000 FT.

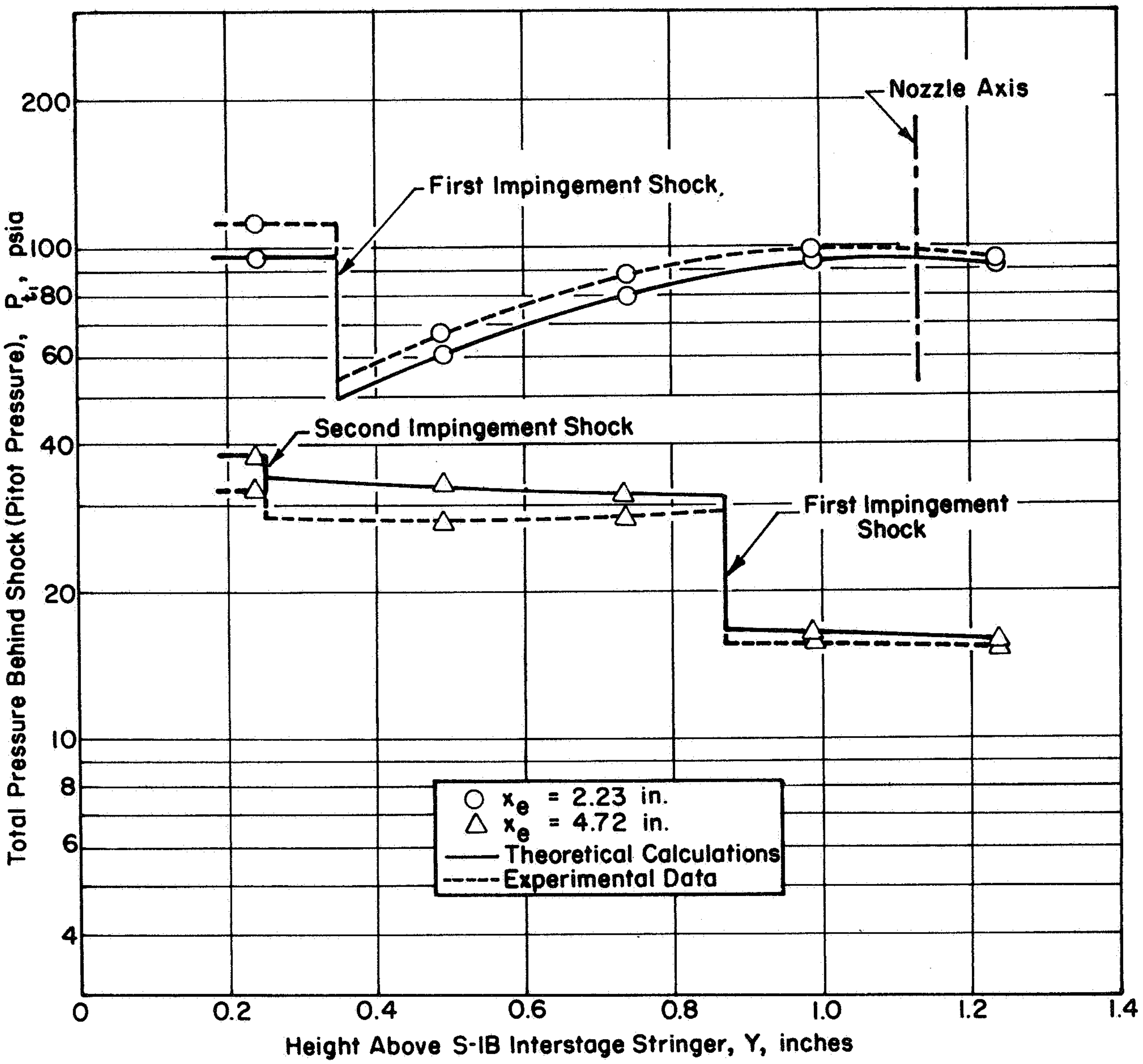

FIGURE 17. COMPARISON OF TOTAL PRESSURE BEHIND SHOCK (PITOT PRESSURE) IN S-IB RETRO MOTOR PLUME AT 200,000 FEET

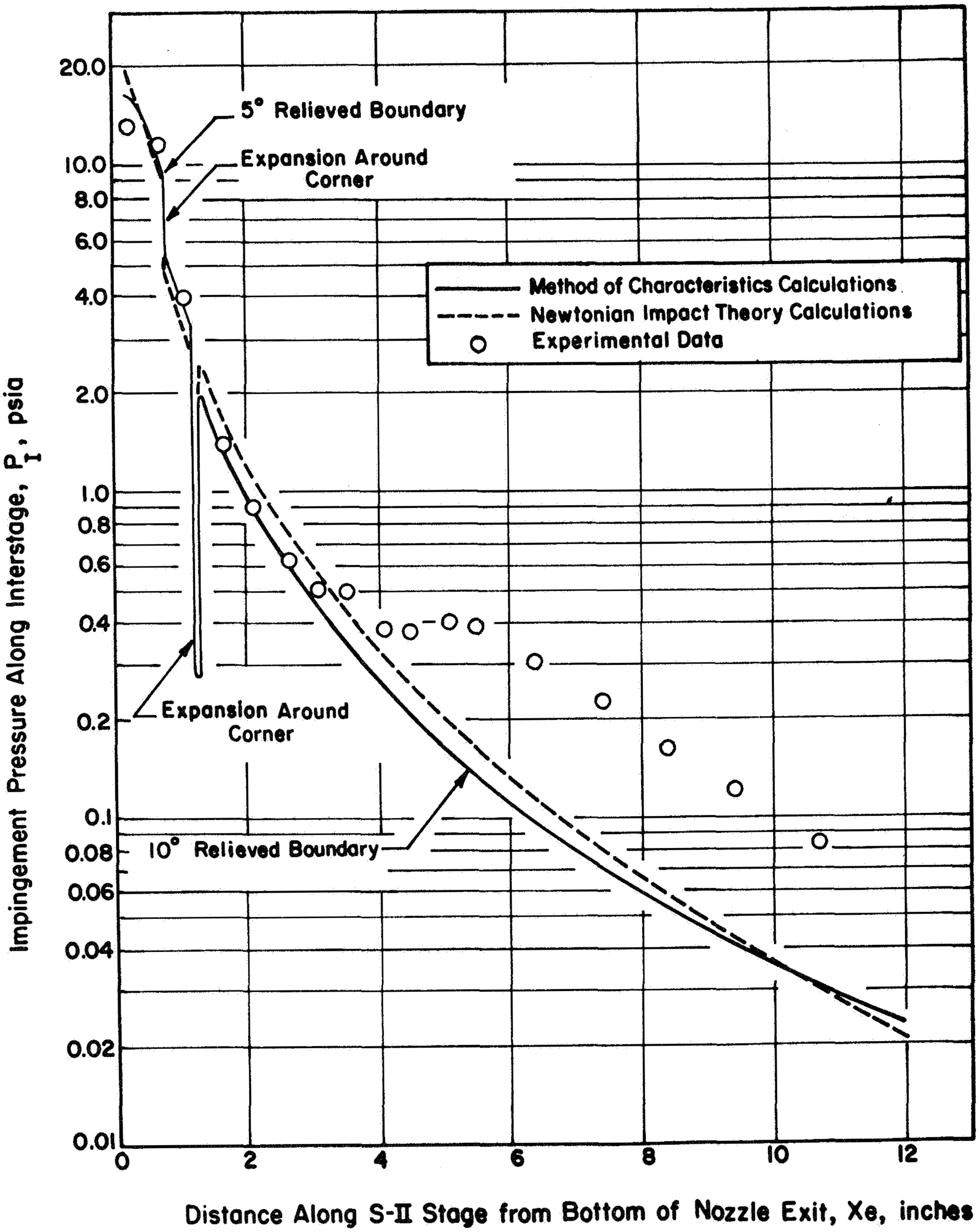

FIGURE 18. COMPARISON OF PRESSURES ON S-II INTERSTAGE DUE TO EXHAUST OF S-II RETRO MOTOR AT 391,000 FEET

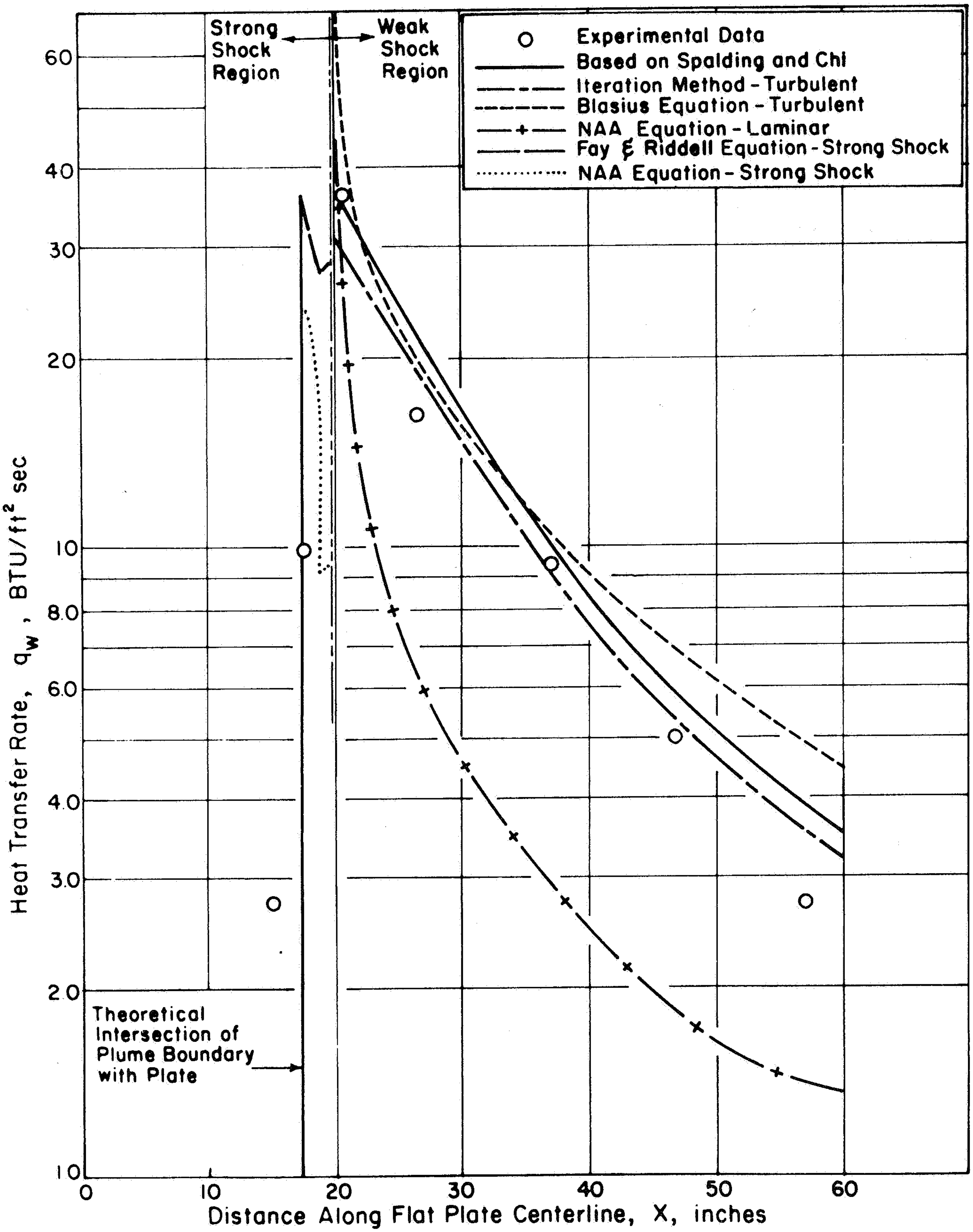

FIGURE 19. COMPARISON OF HEAT TRANSFER RATES ON FLAT PLATE DUE TO EXHAUST OF UTC CENTAUR RETRO MOTOR AT 109,000 FEET

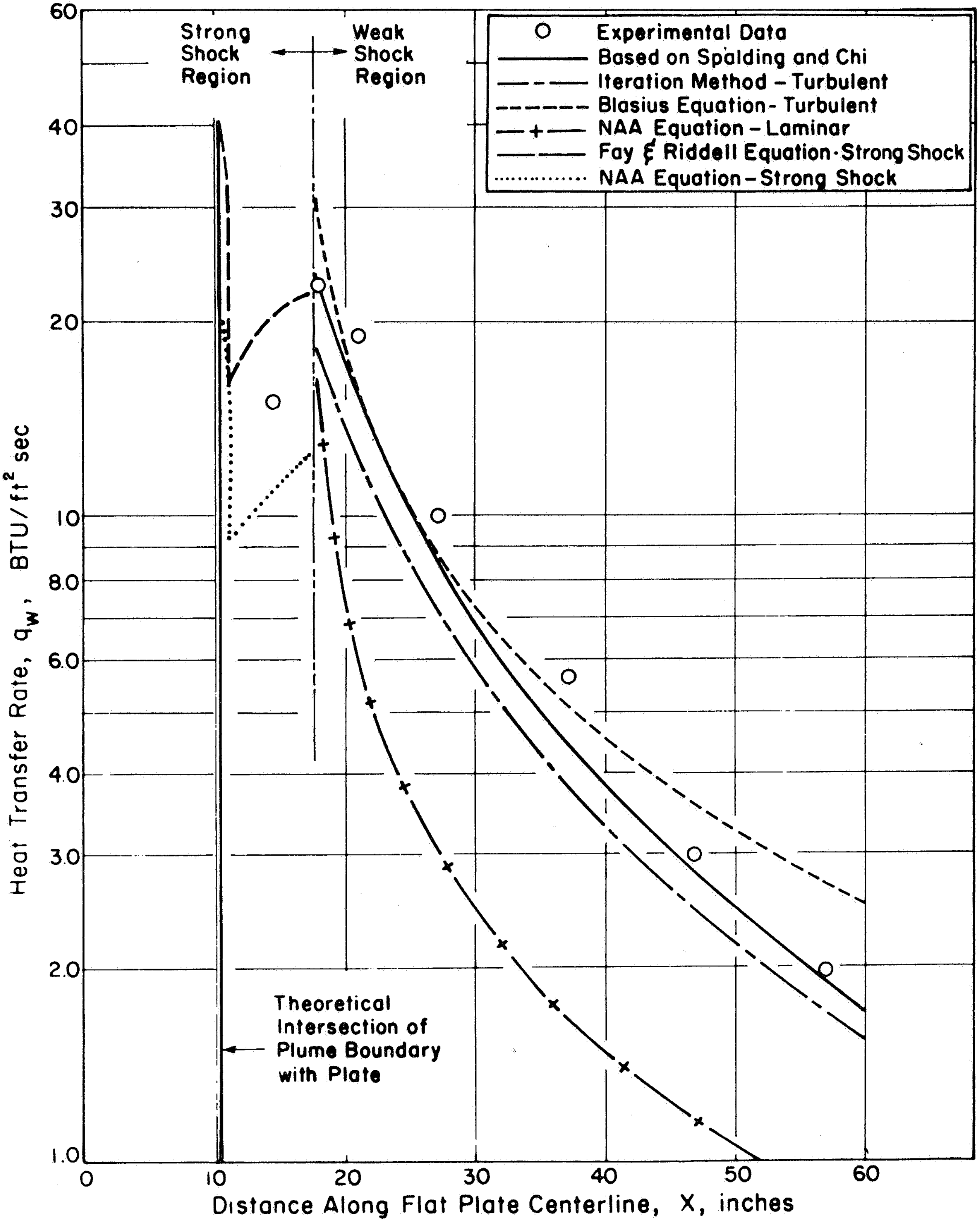

FIGURE 20. COMPARISON OF HEAT TRANSFER RATES ON FLAT PLATE DUE TO EXHAUST OF THIOKOL CENTAUR RETRO MOTOR AT 120,000 FEET

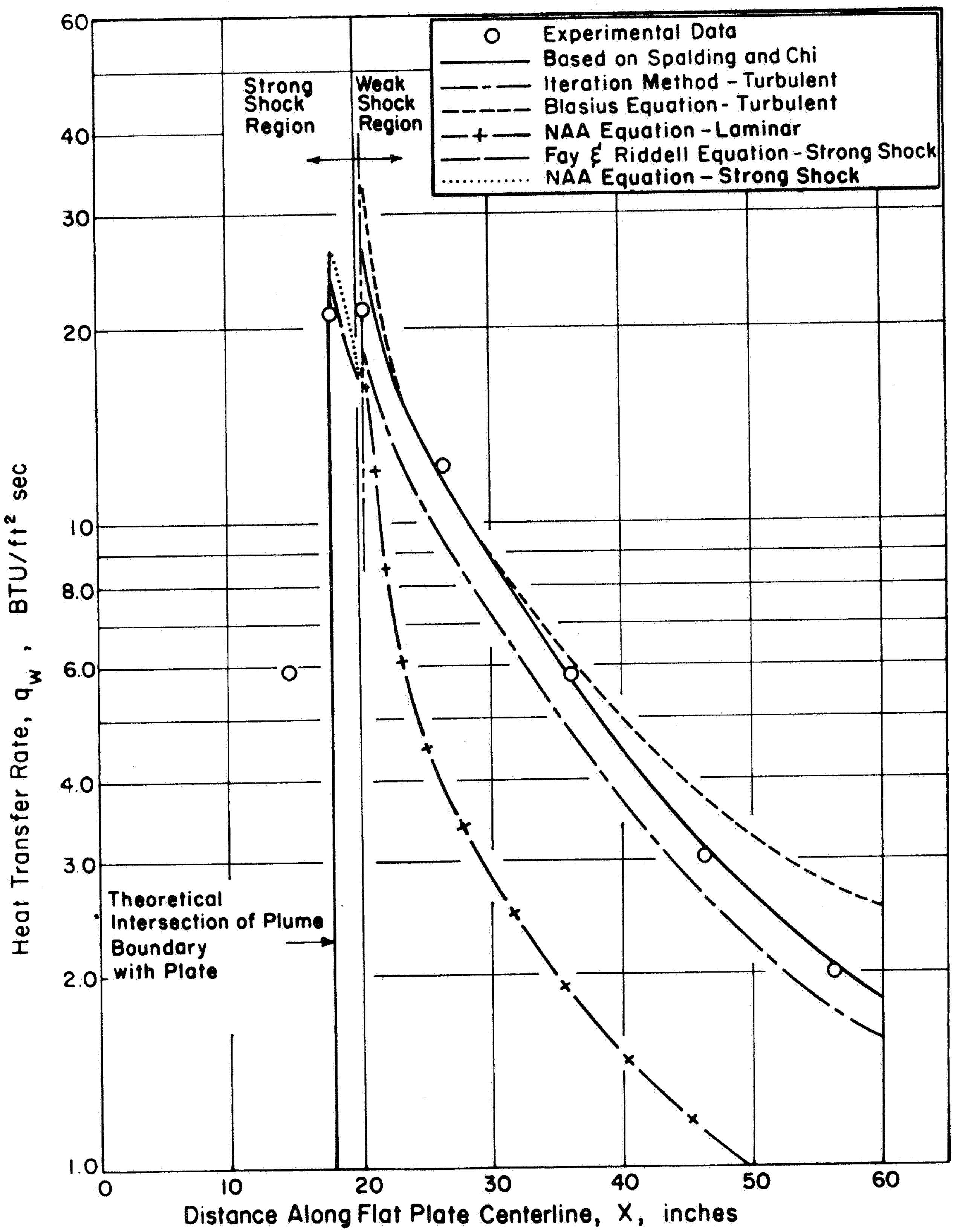

FIGURE 21. COMPARISON OF HEAT TRANSFER RATES ON FLAT PLATE DUE TO EXHAUST OF RPI CENTAUR RETRO MOTOR AT 117,000 FEET

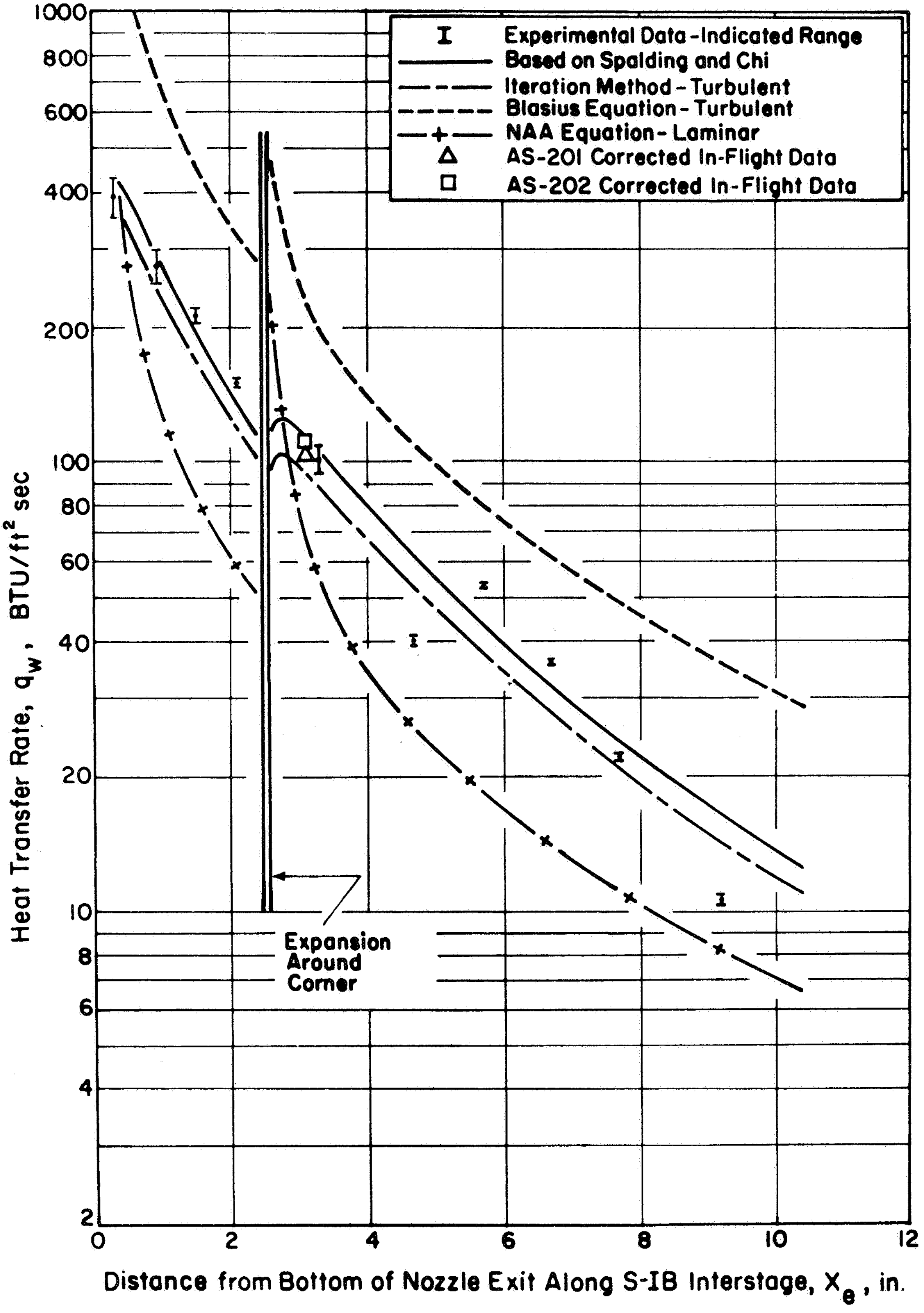

FIGURE 22. COMPARISON OF HEAT TRANSFER RATES ON S-IB INTERSTAGE DUE TO EXHAUST OF S-IB RETRO MOTOR AT 200,000 FEET

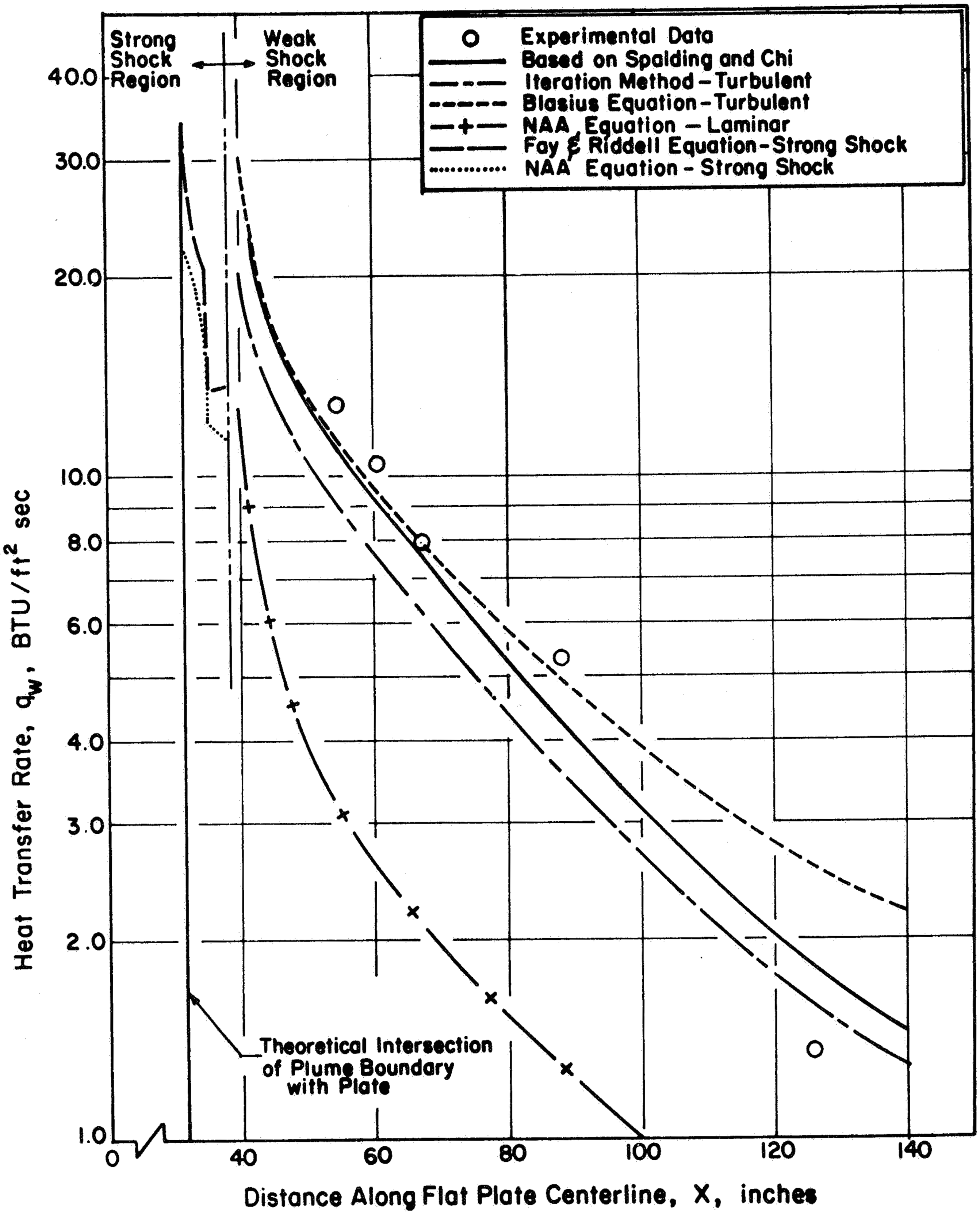

FIGURE 23. COMPARISON OF HEATING RATES ON CENTAUR PANEL DUE TO EXHAUST OF S-IVB RETRO MOTOR AT 115,000 FEET

APPENDIX A

THE CONCEPT OF FAR DOWNSTREAM

Appendix A

THE CONCEPT OF FAR DOWNSTREAM

One of the criteria used in this analysis to establish the flow relief associated with a nozzle exhaust plume impinging on a parallel flat plate is based on an intercepted volume segment of the plume and necessarily contains one arbitrary constant. The constant to be determined is the downstream point along the plume axis of symmetry at which the volume calculation should be terminated and, hence, uniquely define the volume segment for a given case. The location of this downstream point is determined by considering the relationship between "far downstream" and the concept of maximum or "limiting flow relief."

The term designated as flow relief is not well defined, but in this context it is meant to imply the slope of the artificial boundary used in an axisymmetric method-of-characteristics flow field to simulate the true three dimensional spreading of the flow over a flat plate at a particular axial location. From the form of the experimental pressure distribution along the centerline of the flat plate, it was observed that the slope of the artificial boundary producing the distribution approached a constant value, i.e., a limiting value representing the maximum amount of relief needed to simulate the physical problem. From the equation of the relieved boundary

$$(\bar{R} - \bar{h})^3 + a\,(\bar{R} - \bar{h})\,(\bar{x} - \bar{x}_o) - b\,(\bar{x} - \bar{x}_o)^3 = 0 \qquad \text{(A-1)}$$

it is clear that the slope or first derivative asymptotically approaches the value $b^{1/3}$ for increasing $\bar{x}$. If the parameter, $\tan\theta$, is defined

$$\tan\theta = b^{1/3} \qquad \text{(A-2)}$$

then the angle θ is a measure of the maximum or limiting flow relief far downstream.

The volume ratio, V_1/V_2, where

V_1 = volume segment of exhaust plume contained within the undisturbed plume free boundary and the flat plate boundary between $\overline{x}_T$ and $(\overline{x}_T + p_o)$

V_2 = volume of the axisymmetric unrelieved flow field between $\overline{x}_T$ and $(\overline{x}_T + p_o)$

p_o = unknown point far downstream

$\overline{x}_T$ = nondimensional supersonic turning point

is correctly a need for relief rather than a measure of relief. It is important to realize that V_1/V_2 for a given point p_o describes an overall or "gross" estimate of "need" and does not reflect a local distribution for all values of $\overline{x}$ between and $\overline{x}_T$ and $(\overline{x}_T + p_o)$. Hence it should be related to the "gross" measure of relief associated with the artificial boundary equation, $\tan\theta$.

For the range of parameters considered in this analysis

$$\begin{aligned} 0 \le a \le 2.5 \\ 0 \le \tan\theta \le .45 \end{aligned} \qquad \text{(A-3)}$$

the universal far downstream point was taken to be $(\overline{x}_T + 30)$, based on the criteria that the value of the first derivative of Equation (A-1) should be asymptotically close to $\tan\theta$. This is closely satisfied in the four different example cases shown in Figures A1 through A4. It is not meant to imply that the general impingement theory and the relationship between need for relief, V_1/V_2, and the measure of relief, $\tan\theta$, would not be valid for a different downstream point, e.g., $(\overline{x}_T + 35)$. The empirically derived curves would be slightly different, but the prediction method would function equally as well.

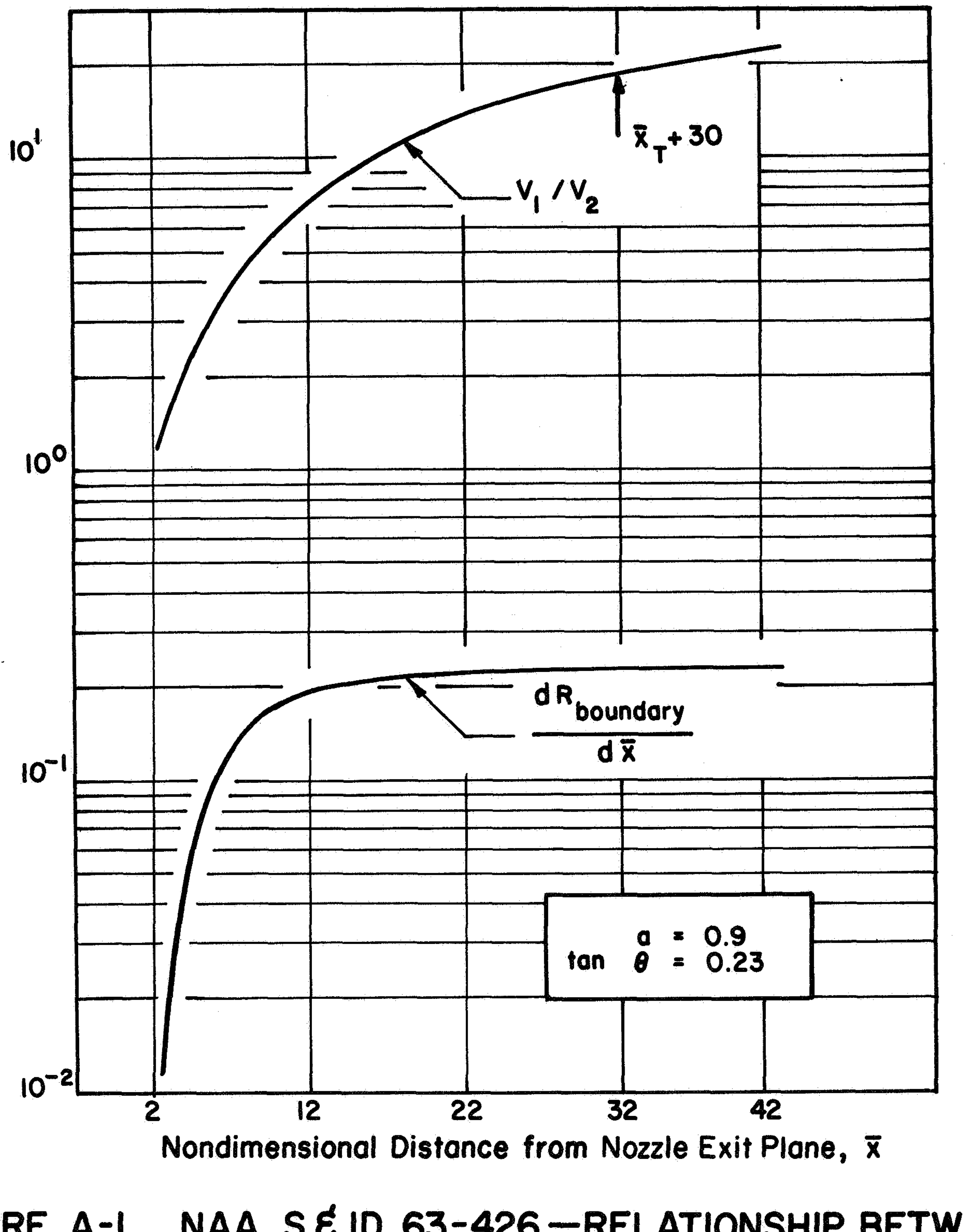

FIGURE A-1. NAA S&ID 63-426—RELATIONSHIP BETWEEN VOLUME RATIO AND DERIVATIVE OF RELIEVED BOUNDARY AS A FUNCTION OF $\bar{x}$

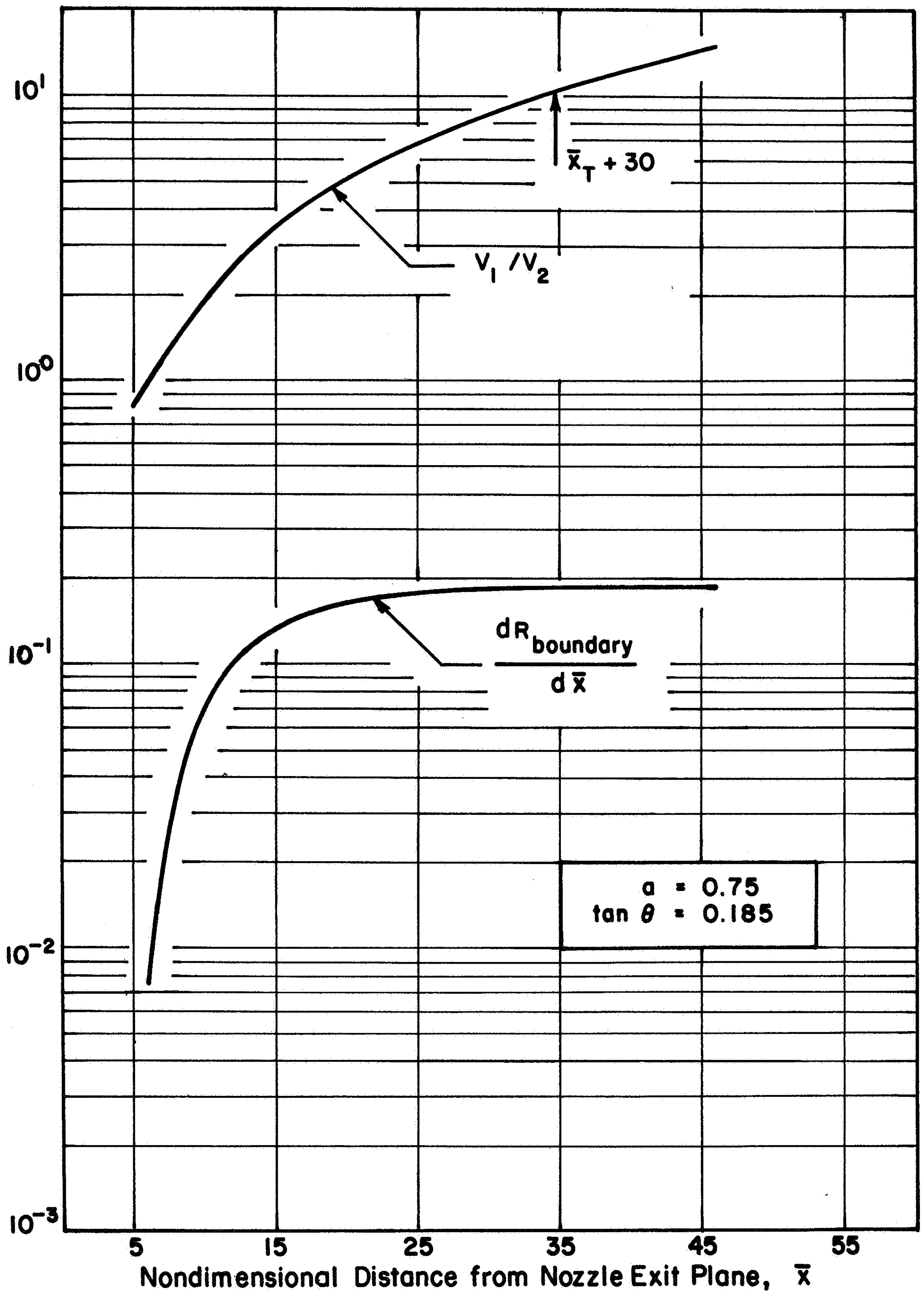

FIGURE A-2. RDS-507—RELATIONSHIP BETWEEN VOLUME RATIO AND DERIVATIVE OF RELIEVED BOUNDARY AS A FUNCTION OF $\bar{x}$

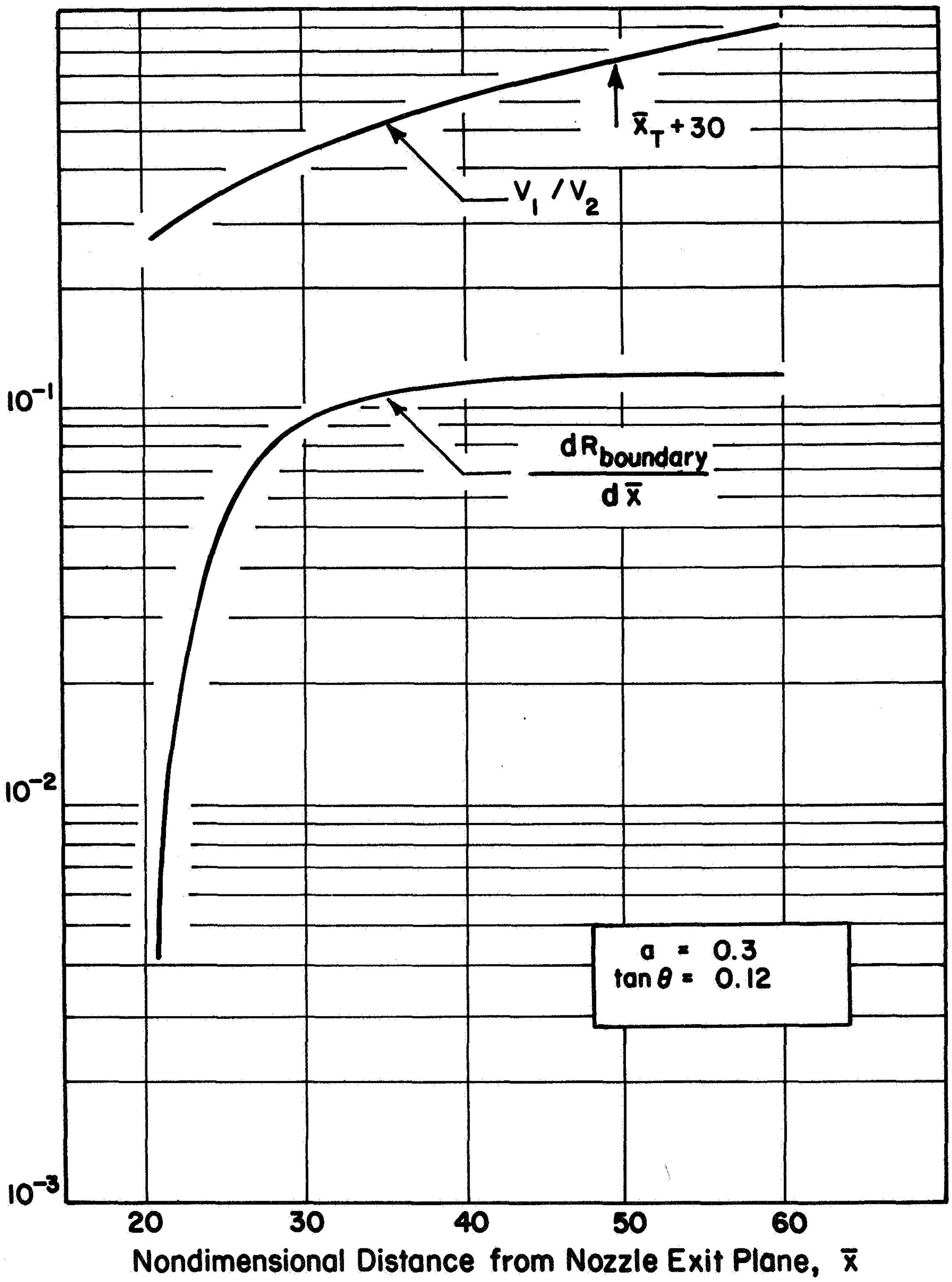

FIGURE A-3. THIOKOL CENTAUR RETRO—RELATIONSHIP BETWEEN VOLUME RATIO AND DERIVATIVE OF RELIEVED BOUNDARY AS A FUNCTION OF $\bar{x}$

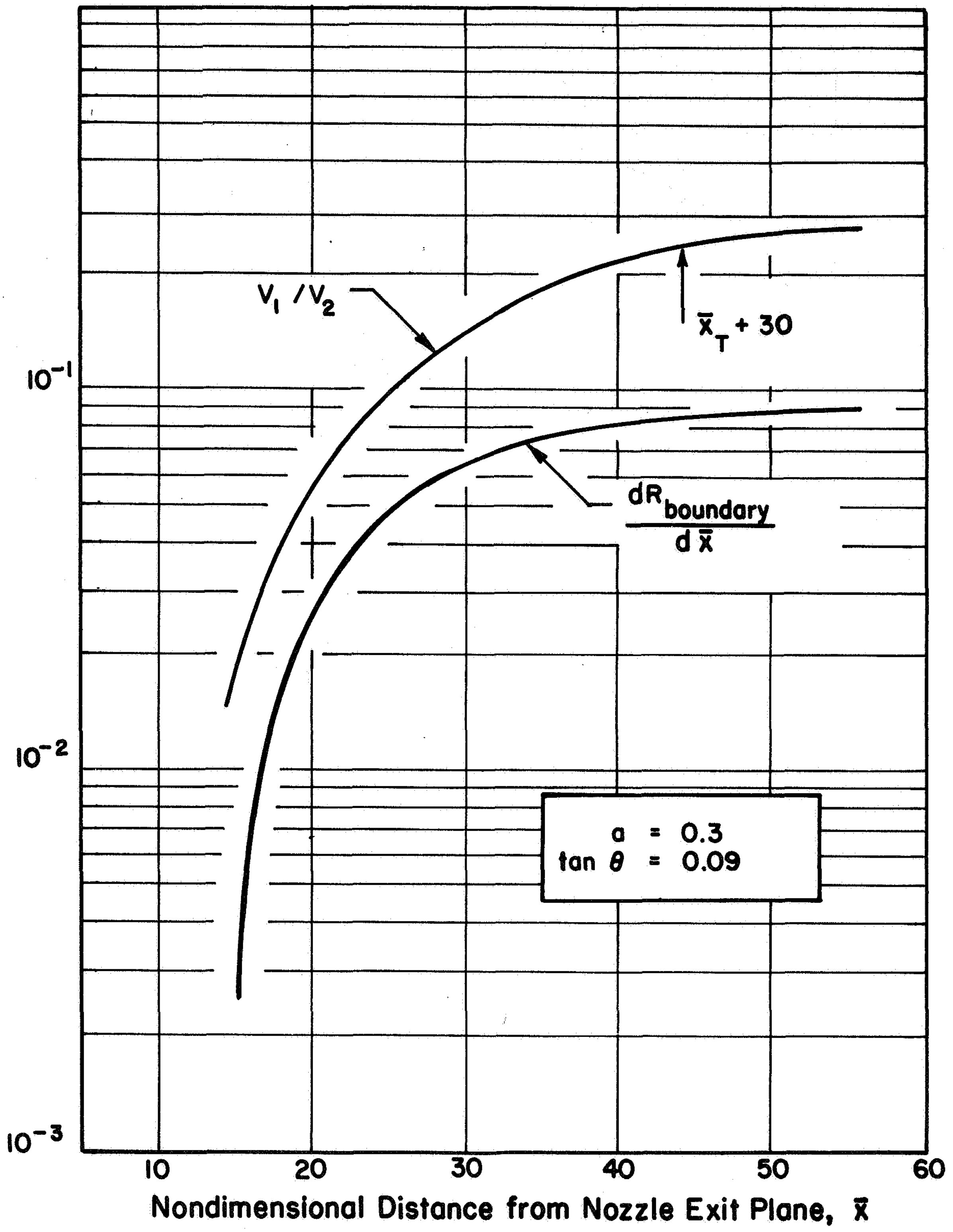

FIGURE A-4. RPI CENTAUR RETRO-RELATIONSHIP BETWEEN VOLUME RATIO AND DERIVATIVE OF RELIEVED BOUNDARY AS A FUNCTION OF $\bar{x}$